



Comparison of the Hall Magnetohydrodynamics and Magnetohydrodynamics Evolution of a Flaring Solar Active Region

K. Bora^{1,2}, R. Bhattacharyya¹, Avijeet Prasad^{3,4,5}, Bhuwan Joshi¹, and Qiang Hu^{3,6}

¹ Udaipur Solar Observatory, Physical Research Laboratory, Dewali, Bari Road, Udaipur 313001, India

² Discipline of Physics, Indian Institute of Technology, Gandhinagar 382355, India

³ Center for Space Plasma & Aeronomic Research, The University of Alabama in Huntsville, Huntsville, AL 35899, USA

⁴ Institute of Theoretical Astrophysics, University of Oslo, Postboks 1029, Blindern NO-0315 Oslo, Norway

⁵ Rosseland Centre for Solar Physics, University of Oslo, Postboks 1029, Blindern NO-0315, Oslo, Norway

⁶ Department of Space Science, The University of Alabama in Huntsville, Huntsville, AL 35899, USA

Received 2021 September 13; revised 2021 November 13; accepted 2021 November 20; published 2022 February 4

Abstract

This work analyzes the Hall magnetohydrodynamics (HMHD) and magnetohydrodynamics (MHD) numerical simulations of a flaring solar active region as a test bed while idealizing the coronal Alfvén speed to be less by two orders of magnitude. HMHD supports faster magnetic reconnection and shows richer complexity in magnetic field line evolution compared to the MHD. The magnetic reconnections triggering the flare are explored by numerical simulations augmented with relevant multiwavelength observations. The initial coronal magnetic field is constructed by non-force-free extrapolation of photospheric vector magnetic field. Magnetic structure involved in the flare is identified to be a flux rope, with its overlying magnetic field lines constituting the quasi-separatrix layers (QSLs) along with a three-dimensional null point and a null line. Compared to the MHD simulation, the HMHD simulation shows a higher and faster ascent of the rope together with the overlying field lines, which further reconnect at the QSL located higher up in the corona. The footpoints of the field lines match better with the observations for the HMHD case, with the central part of the flare ribbon located at the chromosphere. Additionally, field lines are found to rotate in a circular pattern in the HMHD, whereas no such rotation is seen in the MHD results. Interestingly, plasma is also observed to be rotating in a cospatial chromospheric region, which makes the HMHD simulation more credible. Based on the aforementioned agreements, HMHD simulation is found to agree better with observations and thus opens up a novel avenue to explore.

Unified Astronomy Thesaurus concepts: Solar magnetic reconnection (1504); Magnetohydrodynamical simulations (1966)

Supporting material: animations

1. Introduction

The astrophysical plasmas characterized by high Lundquist number $S \equiv L\nu_A/\eta$ ($L \equiv$ length scale of the magnetic field \mathbf{B} variability, $\nu_A \equiv$ Alfvén speed, and $\eta \equiv$ magnetic diffusivity) satisfy Alfvén’s flux-freezing theorem in the presence of laminar plasma flow, ensuring that magnetic field lines are tied to fluid parcels (Alfvén 1942). The scenario is different in a turbulent magnetofluid; see Lazarian & Vishniac (1999, 2000) and Eyink & Aluie (2006) for details. An inherent large L implies large S and ensures flux freezing in the astrophysical plasmas. Particularly, the solar corona with global $L \approx 100$ Mm, $\nu_A \approx 10^6$ ms^{−1}, $B \approx 10$ G, and $\eta \approx 1$ m² s^{−1} (calculated using Spitzer resistivity) has $S \approx 10^{14}$ (Aschwanden 2005). However, the coronal plasma also exhibits diffusive behavior in the form of solar transients—such as solar flares, coronal mass ejections, and jets. All of these are manifestations of magnetic reconnections that in turn lead to dissipation of magnetic energy into heat and kinetic energy of plasma flow, accompanied by a rearrangement of magnetic field lines (Choudhuri 1998). The magnetic reconnections being dissipative processes, their onset is due to the generation of small scales as a consequence of large-scale dynamics, ultimately increasing the magnetic field gradient and thereby resulting in

intermittently diffusive plasma. The small scales may naturally occur as current sheets (CSs; Parker 1994), magnetic nulls (Parnell et al. 1996; Nayak et al. 2020), and quasi-separatrix layers (QSLs; Démoulin 2006; Prasad et al. 2020), or can develop spontaneously during the evolution of the magnetofluid. Such spontaneous developments (owing to discontinuities in the magnetic field) are expected from Parker’s magnetostatic theorem (Parker 1994) and have also been established numerically by magnetohydrodynamics (MHD) simulations (Kumar & Bhattacharyya 2011; Kumar et al. 2015, 2016, 2017, 2021; Prasad et al. 2017, 2018; Nayak et al. 2019, 2020). Identification of the small (viz., the dissipation) scale depends on the specific physical system under consideration. For example, the length scale at which the reconnection occurs is found to be $L_\eta \equiv \sqrt{\tau_d \eta} \approx 32$ m, based on $\eta \approx 1$ m² s^{−1} and the magnetic diffusion timescale τ_d approximated by the impulsive rise time of hard X-ray flux $\approx 10^3$ s (Priest & Forbes 2000) during a flare. Consequently, the estimated ion inertial length scale $\delta_i \approx 2.25$ m in the solar corona (Priest & Forbes 2000) suggests that the order of the dissipation term, $1/S \approx 10^{-5}$ (approximated with L_η), is smaller than the order of the Hall term, $\delta_i/L_\eta \approx 10^{-2}$, in the standard dimensionless induction equation (Westerberg & Åkerstedt 2007; Bora et al. 2021)

$$\frac{\partial \mathbf{B}}{\partial t} = \nabla \times (\mathbf{v} \times \mathbf{B}) - \frac{1}{S} \nabla \times \mathbf{J} - \frac{\delta_i}{L_\eta} \nabla \times (\mathbf{J} \times \mathbf{B}), \quad (1)$$

where $\mathbf{J}(\mathbf{r}) = \nabla \times \mathbf{B}$ and \mathbf{v} are the volume current density and the plasma flow velocity, respectively. This difference in the order of magnitude irrefutably indicates the importance of the Hall term in the diffusive limit (Birn et al. 2001; Bhattacharjee 2004) of the solar coronal plasma, which further signifies that the Hall magnetohydrodynamics (HMHD) can play a crucial role for coronal transients, as the magnetic reconnections are their underlying mechanism. Importantly, the aforesaid activation of the Hall term only in the diffusive limit is crucial in setting up an HMHD-based numerical simulation, invoked later in the paper.

Important insight into magnetic reconnection can be gained by casting Equation (1) in the absence of dissipation as

$$\frac{\partial \mathbf{B}}{\partial t} = \nabla \times (\mathbf{w} \times \mathbf{B}), \quad (2)$$

following Hornig & Schindler (1996). The velocity $\mathbf{w} = \mathbf{v} - \delta_i/L_p \mathbf{J}$, which is also the electron fluid velocity, conserves magnetic flux (Schindler et al. 1988) and topology (Hornig & Schindler 1996) since field lines are tied to it. Consequently, field lines slip out from the fluid parcels advecting with velocity \mathbf{v} to which the lines are frozen in ideal MHD. Importantly, the resulting breakdown of the flux freezing is localized to the region where current density is large and the Hall term is effective. Because of the slippage, two fluid parcels do not remain connected with the same field lines over time—a change in field line connectivity. Quoting Schindler et al. (1988), such localized breakdown of flux freezing, along with the resulting change in connectivity, can be considered as the basis of reconnection (Axford 1984). Additional slippage of field lines occurs in the presence of the dissipation term, but with a change in magnetic topology. The present paper extensively relies on this interpretation of reconnection as the slippage of magnetic field lines and the resulting change in magnetic connectivity.

The importance of HMHD is by no means limited to coronal transients. For example, HMHD is important in Earth’s magnetosphere, particularly at the magnetopause and the magnetotail, where CSs are present (Mozer et al. 2002). Generally, the HMHD is expected to support faster magnetic reconnections, yet without directly affecting the dissipation rate of magnetic energy and helicity by the Hall term in the induction equation (Priest & Forbes 2000; Shi et al. 2019). The faster reconnection may be associated with a more effective slippage of field lines in HMHD compared to the resistive MHD, compatible with the arguments presented earlier. Nevertheless, these unique properties of the HMHD are expected to bring subtle changes in the dynamical evolution of plasma, particularly in the small scales dominated by magnetic reconnections, presumably bringing a change in the large scales as a consequence. Such subtle changes were found in the recent HMHD simulation (Bora et al. 2021), performed by extending the computational model EULAG-MHD (Smolarkiewicz & Charbonneau 2013) to include the Hall effects. Notably, the faster reconnection compared to MHD led to a breakage of a magnetic flux rope, generated from analytically constructed initial bipolar magnetic field lines (Kumar et al. 2016). In turn, the flux-rope breakage resulted in the generation of magnetic islands as theorized by Shibata & Tanuma (2001). Clearly, it is compelling to study the HMHD evolution in a more

realistic scenario with the initial magnetic field obtained from a solar magnetogram. To attain such an objective, we select the recently reported active region (AR) NOAA AR 12734 by Joshi et al. (2021) that produced a C1.3 class flare.

In the absence of reliable direct measurement of the coronal magnetic field, several extrapolation models such as nonlinear force-free field (NLFFF) (Wiegmann 2008; Wiegmann & Sakurai 2012) and non-force-free field (non-FFF) (Hu & Dasgupta 2008; Hu et al. 2010) have been developed to construct the coronal magnetic field using photospheric magnetograms. The standard is the NLFFF, and the recent data-based MHD simulations initialized with it have been reasonably successful in simulating the dynamics of various coronal transients (Jiang et al. 2013; Amari et al. 2014; Inoue et al. 2014; Savcheva et al. 2016). However, the NLFFF extrapolations require that we treat the photosphere as force-free, while it is actually not so (Gary 2001). Hence, a “preprocessing technique” is usually employed to minimize the Lorentz force on the photosphere in order to provide a boundary condition suitable for NLFFF extrapolations (Wiegmann et al. 2006; Jiang & Feng 2014) and thereby compromising the reality. Recently, the non-FFF model, based on the principle of minimum energy dissipation rate (Bhattacharyya & Janaki 2004; Bhattacharyya et al. 2007), has emerged as a plausible alternative to the force-free models (Hu & Dasgupta 2008; Hu et al. 2008, 2010). In the non-FFF model, the magnetic field \mathbf{B} satisfies the double-curl Beltrami equation (Mahajan & Yoshida 1998), and the corresponding Lorentz force on the photosphere is nonzero, while it decreases to small values at the coronal heights (Prasad et al. 2018, 2020; Nayak et al. 2019)—concurring with the observations. In this paper, we use non-FFF extrapolation (Hu et al. 2010) to obtain the magnetic field in the corona using the photospheric vector magnetogram obtained from the Helioseismic Magnetic Imager (HMI; Schou et al. 2012) on board the Solar Dynamics Observatory (SDO; Pesnell et al. 2012).

The paper is organized as follows. Section 2 describes the flaring event in NOAA AR 12734, Section 3 presents the magnetic field line morphology of NOAA AR 12734, along with the preferable sites for magnetic reconnections such as QSLs, 3D null point, and null line found from the non-FFF extrapolation. Section 4 focuses on the numerical model, numerical setup, and evolution of magnetic field lines obtained from the extrapolation, along with their realizations in observations. Section 5 highlights the key findings.

2. Salient Features of the C1.3 Class Flare in NOAA AR 12734

NOAA AR 12734 produced an extended C1.3 class flare on 2019 March 8 (Joshi et al. 2021). The impulsive phase of the flare started at 03:07 UT as reported in Figure 3 of Joshi et al. (2021), which shows the X-ray flux in 1–8 Å and 0.5–4 Å detected by the Geostationary Operational Environmental Satellite (GOES; Garcia 1994). The flux evinces two subsequent peaks after the onset of the flare, one around 03:19 UT and another roughly around 03:38 UT. Joshi et al. (2021) suggested that the eruptive event takes place in a coronal sigmoid with two distinct stages of energy release. Additional observations using the multiwavelength channels of the Atmospheric Imaging Assembly (AIA; Lemen et al. 2012) on board SDO are listed below to highlight important features pertaining to simulations reported in this paper. Figure 1

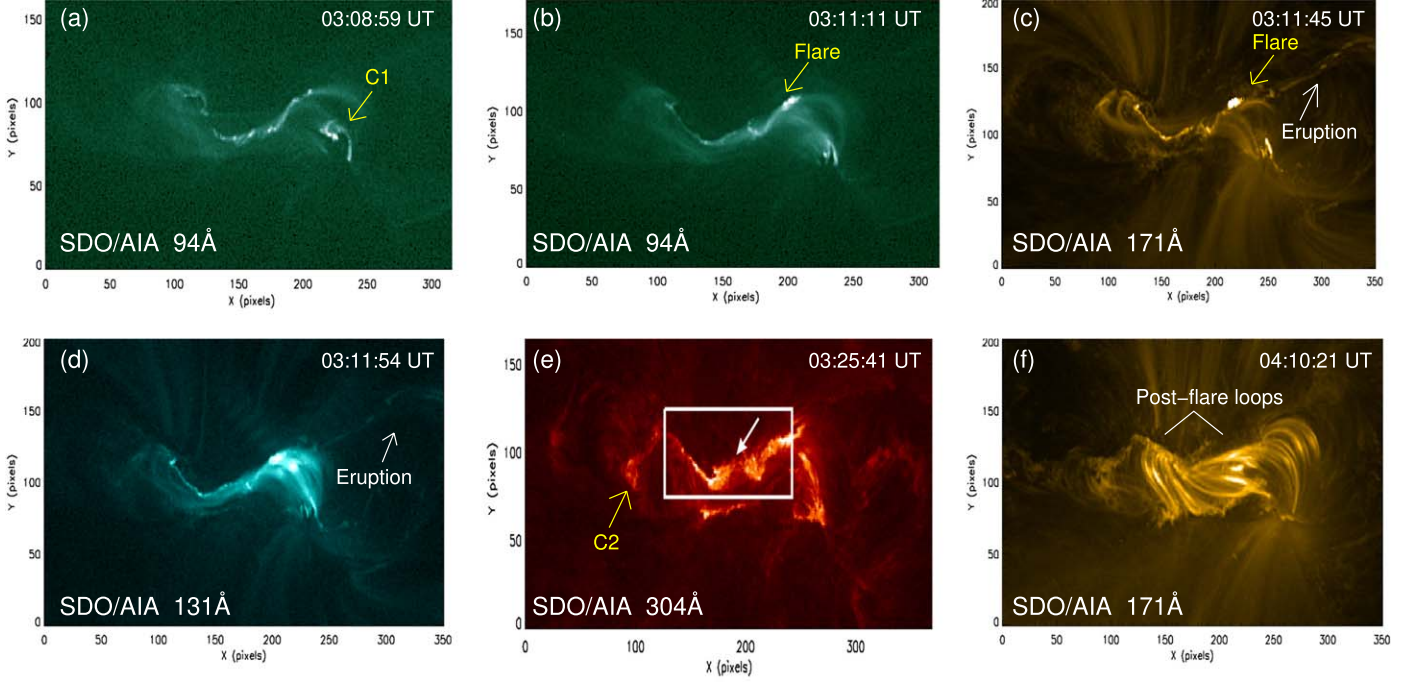


Figure 1. Panels (a)–(f) are SDO/AIA images showing the multiwavelength observations of the flaring NOAA AR 12734. Panel (a) shows the quasi-circular brightening at the western part of the AR prior to the flare (marked by C1). Panels (b)–(d) show the initiation of the flare followed by eruption (indicated by the yellow arrow). Panel (e) shows the circular structure after eruption at the eastern part of the AR (marked by C2) and the W-shaped flare ribbon (enclosed by the white box). Panel (f) shows the post-flare loops.

illustrates a spatio-temporal observational overview of the event. Panel (a) shows the remote semicircular brightening (C1) prior to the impulsive phase of the flare (indicated by the yellow arrow). Panels (b)–(d) indicate the flare by the yellow arrow and the eruption by the white arrow in the 94 Å, 171 Å, and 131 Å channels, respectively. Notably, the W-shaped brightening appears in panels (b)–(d), along with the flare in different wavelength channels of SDO/AIA. Panel (e) shows the circular structure of the chromospheric material (C2) during the impulsive phase of the flare. It also highlights the developed W-shaped flare ribbon (enclosed by the white box), which has a tip at the center (marked by the white arrow). Panel (f) depicts the post-flare loops in the 171 Å channel, indicating the post-flare magnetic field line connectivity between various negative and positive polarities on the photosphere.

3. Non-FFF Extrapolation of NOAA AR 12734

As stated up front, the non-FFF extrapolation technique proposed by Hu & Dasgupta (2008) and based on the minimum dissipation rate theory (Bhattacharyya & Janaki 2004; Bhattacharyya et al. 2007) is used to obtain the coronal magnetic field for NOAA AR 12734. The extrapolation essentially solves the equation

$$\nabla \times \nabla \times \nabla \times \mathbf{B} + a_1 \nabla \times \nabla \times \mathbf{B} + b_1 \nabla \times \mathbf{B} = 0, \quad (3)$$

where parameters a_1 and b_1 are constants. Following Hu et al. (2010), the field is constructed as

$$\mathbf{B} = \sum_{i=1,2,3} \mathbf{B}_i, \quad \nabla \times \mathbf{B}_i = \alpha_i \mathbf{B}_i, \quad (4)$$

where α_i is constant for a given \mathbf{B}_i . The subfields \mathbf{B}_1 and \mathbf{B}_3 are linear force-free, having $\alpha_1 \neq \alpha_3$, whereas \mathbf{B}_2 is a potential field with $\alpha_2 = 0$. An optimal pair of $\alpha = \{\alpha_1, \alpha_3\}$ is iteratively

found by minimizing the average deviation between the observed transverse field (\mathbf{B}_t) and the computed (\mathbf{b}_t) transverse field, quantified by

$$E_n = \left(\sum_{i=1}^M |\mathbf{B}_{t,i} - \mathbf{b}_{t,i}| \times |\mathbf{B}_{t,i}| \right) / \left(\sum_{i=1}^M |\mathbf{B}_{t,i}|^2 \right), \quad (5)$$

on the photosphere. Here $M = N^2$ represents the total number of grid points on the transverse plane. The grid points are weighted with respect to the strength of the observed transverse field to minimize the contribution from weaker fields, see Hu & Dasgupta (2008) and Hu et al. (2010) for further details.

Since Equation (3) involves the evaluation of the second-order derivative, $(\nabla \times \nabla \times \mathbf{B})_z = -(\nabla^2 \mathbf{B})_z$ at $z = 0$, evaluation of \mathbf{B} requires magnetograms at two different values of z . In order to work with the generally available single-layer vector magnetograms, an algorithm was introduced by Hu et al. (2010) that involves additional iterations to successively fine-tune the potential subfield \mathbf{B}_2 . The system is reduced to second order by taking initial guess $\mathbf{B}_2 = 0$, which makes it easier to determine the boundary condition for \mathbf{B}_1 and \mathbf{B}_3 . If the calculated value of E_n turns out to be unsatisfactory—i.e., overly large—then a potential field corrector to \mathbf{B}_2 is calculated from the difference in the observed and computed transverse fields and subsequently summed with the previous \mathbf{B}_2 to further reduce E_n . Notably, recent simulations initiated with the non-FFF model have successfully explained the circular ribbon flares in NOAA AR 12192 (Prasad et al. 2018) and NOAA AR 11283 (Prasad et al. 2020), as well as a blowout jet in NOAA AR 12615 (Nayak et al. 2019), thus validating the non-FFF model’s credibility.

The vector magnetogram is selected for 2019 March 8, at 03:00 UT (≈ 7 minutes prior to the start of flare). The original

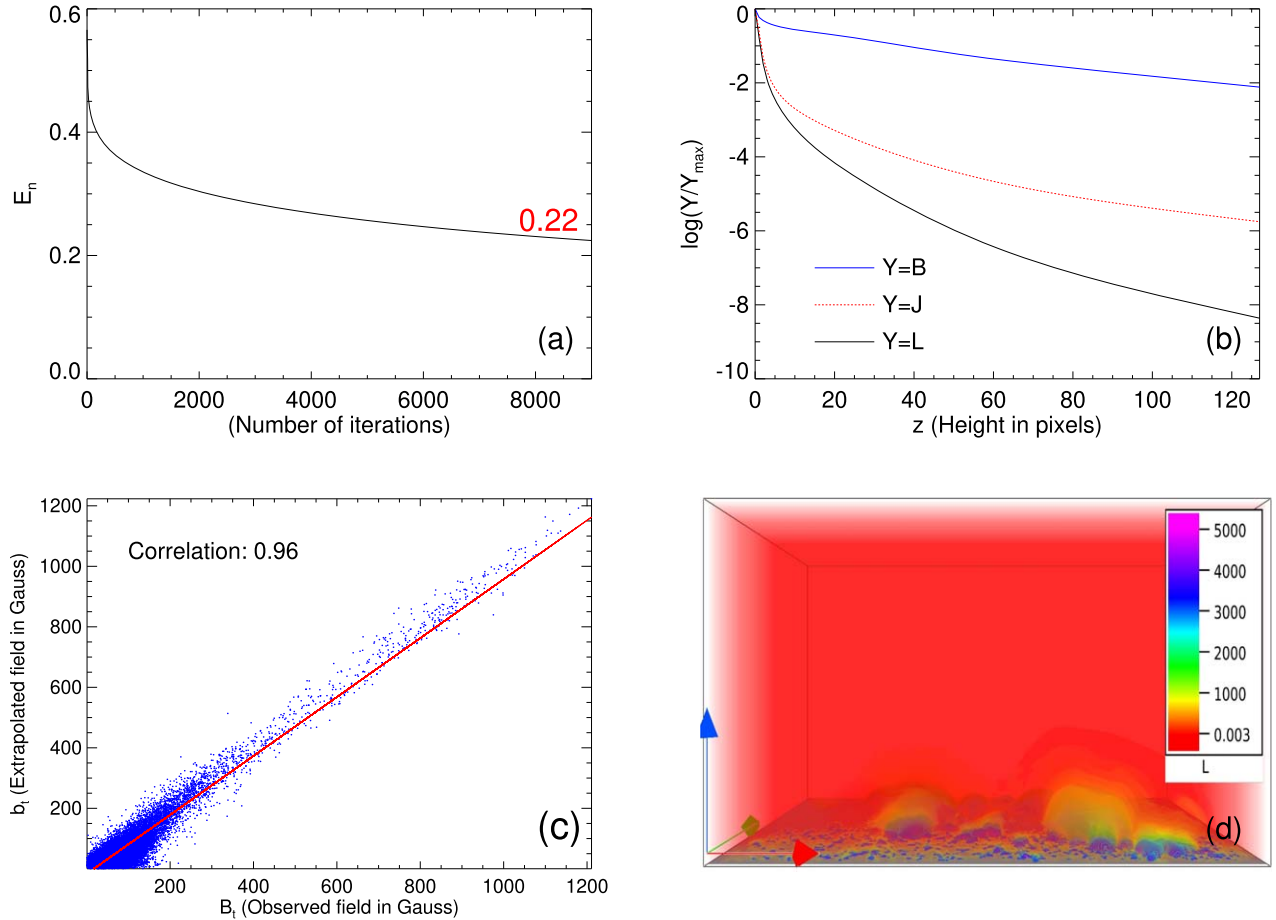


Figure 2. Panel (a) shows the variation of the deviation E_n with number of iterations in the non-FFF extrapolation. Panel (b) shows the logarithmic variation of horizontally averaged magnetic field ($Y=B$), the current density ($Y=J$), and the Lorentz force ($Y=L$) with height z in pixels. All the quantities plotted in panel (b) are normalized with their respective maximum values. Panel (c) shows the scatter plot of the correlation between the observed and extrapolated magnetic field. The red line is the expected profile for perfect correlation. Distribution of the magnitude of the Lorentz force for initial extrapolated field is shown in panel (d) using direct volume rendering. The distribution clearly shows that the Lorentz force is maximum at the bottom boundary and decreasing with the height in computational volume. The red, green, and blue arrows in the lower left corner represent x -, y -, and z -directions, respectively, here and hereafter. The color bars on the right side of the panel represent the magnitude of the strength of Lorentz force.

magnetogram cut out of dimensions 342×195 pixels with pixel resolution $0''.5 \text{ pixel}^{-1}$ having an extent of $124 \text{ Mm} \times 71 \text{ Mm}$ ⁷ from the “hmi.sharp_cea_720s” series is considered, which ensures an approximate magnetic flux balance at the bottom boundary. To optimize the computational cost with the available resources, the original field is rescaled and non-FFF-extrapolated over a volume of $256 \times 128 \times 128$ pixels while keeping the physical extent the same and preserving all magnetic structures throughout the region. The reduction, in effect, changes the conversion factor of 1 pixel to $\approx 0.484 \text{ Mm}$ along x and $\approx 0.554 \text{ Mm}$ along the y - and z -directions of the employed Cartesian coordinate system.

Panel (a) of Figure 2 shows E_n in the transverse field, defined in Equation (5), as a function of the number of iterations. It shows that E_n tends to saturate at the value of ≈ 0.22 . Panel (b) of Figure 2 shows the logarithmic decay of the normalized horizontally averaged magnetic field, current density, and Lorentz force with height. It is clear that the Lorentz force is appreciable on the photosphere but decays off rapidly with height, agreeing with the general perception that the corona is force-free while the photosphere is not (Liu et al. 2020;

Sarp Yalim et al. 2020). Panel (c) shows that the Pearson- r correlation between the extrapolated and observed transverse fields is ≈ 0.96 , implying strong correlation. The direct volume rendering of the Lorentz force in panel (d) also reveals a sharp decay of the Lorentz force with height, expanding on the result of panel (b).

To facilitate description, Figure 3(a) shows the SDO/AIA 304 Å image at 03:25 UT, where the flare ribbon brightening has been divided into four segments marked as B1–B4. Figure 3(b) shows the initial global magnetic field line morphology of NOAA AR 12734, partitioned into four regions R1–R4, corresponding to the flare ribbon brightening segments B1–B4. The bottom boundary of panel (b) is composed of B_z maps in gray scale, where the lighter shade indicates positive-polarity regions and the darker shade marks negative-polarity regions. The magnetic field line topologies and structures belonging to a specific region and contributing to the flare are documented below.

Region R1: The top-down view of the global magnetic field line morphology is shown in panel (a) of Figure 4. To help locate QSLs, the bottom boundary is overlaid with the log Q map of the squashing factor Q (Liu et al. 2016) in all panels of the figure. Distribution of high Q values along with B_z on the bottom boundary helps in identifying differently connected

⁷ At a distance of 1 au, an angular diameter of $1''$ represents 0.725 Mm on the Sun.

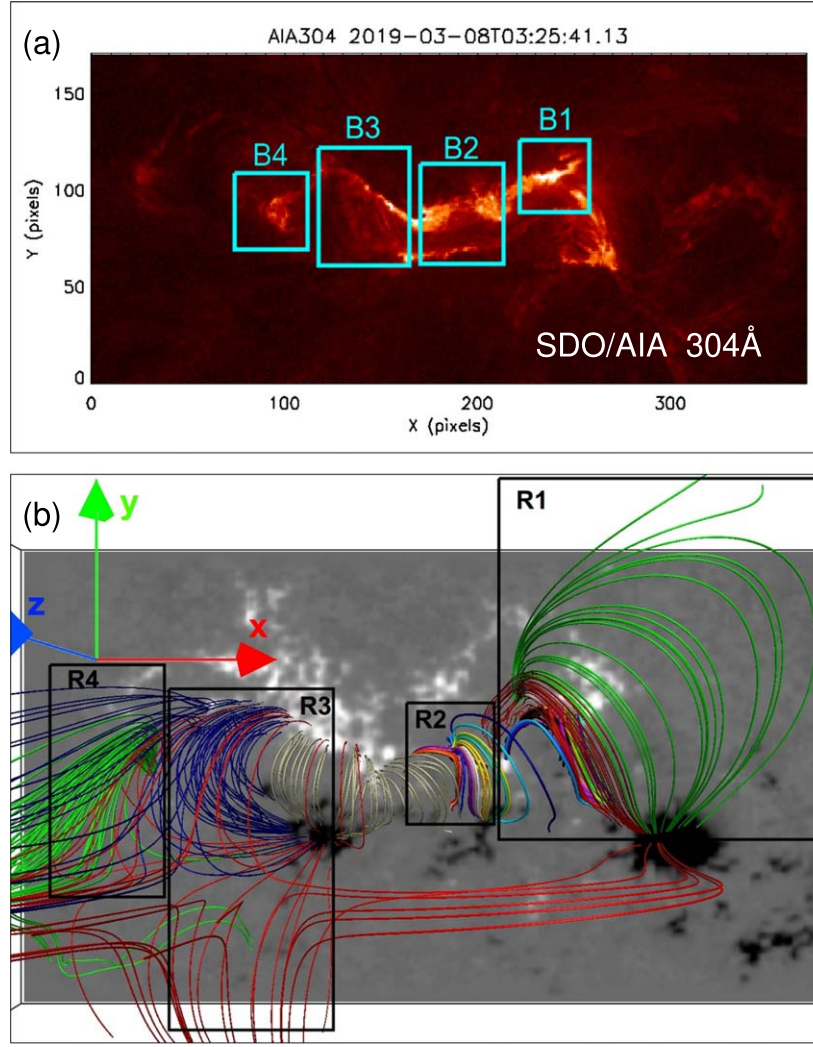


Figure 3. Panel (a) shows the SDO/AIA 304 Å image, where the flare ribbon brightening has been divided into four parts B1, B2, B3, and B4 (enclosed by boxes). Panel (b) shows an overall extrapolated magnetic field lines morphology of NOAA AR 12734 with the B_z -component of the magnetogram at the bottom boundary. Footpoints of the magnetic structures contained in regions R1, R2, R3, and R4 correspond to brightening B1, B2, B3, and B4, respectively.

regions. The region with a large Q is prone to the onset of slipping magnetic reconnections (Démoulin 2006). Footpoints of magnetic field lines constituting QSL1 and QSL2 trace along the high Q values near the bottom boundary. QSL1, involving the magnetic field lines in Set I (green) and Set II (maroon), is shown in panel (b). Particularly, Set I (green) extends higher in the corona, forming the largest loops in R1. Panel (c) illustrates a closer view of QSL2 (multicolored) and the flux rope (black) beneath, situated between the positive and negative polarities P1, P2, and N1, respectively. In panel (d), the flux rope (constituted by the twisted black magnetic field lines) is depicted using the side view. The twist value T_w (Liu et al. 2016) in the three vertical planes along the cross section of the flux rope is also overlaid. Notably, the twist value is 2 at the center of the rope and decreases outward (see vertical plane in the middle of the flux rope in panel (d)).

Region R2: Figure 5(a) shows the side view of a 3D null-point geometry of magnetic field lines and the bottom boundary B_z overlaid with $\log Q$ ranging between 5 and 10. Panel (b) depicts an enlarged view of the 3D null location, marked black. The height of the null is found to be ≈ 3 Mm from the photosphere. The null is detected using the bespoke procedure

(Kumar & Bhattacharyya 2011; Nayak et al. 2020) that approximates the Dirac delta on the grid as

$$n(B_i) = \exp \left[- \sum_{i=x,y,z} (B_i - B_o)^2 / d_o^2 \right], \quad (6)$$

where small constants B_o and d_o correspond to the isovalue of B_i and the Gaussian spread. The function $n(B_i)$ takes significant values only if $B_i \approx 0 \forall i$, whereupon a 3D null is the point where the three isosurfaces having isovalues $B_i = B_o$ intersect.

Region R3: The side view of the magnetic field line morphology in region R3 is shown in Figure 5(c), where the yellow surface corresponds to $n = 0.9$. Panel (d) highlights a “fish-bone-like” structure, similar to the schematic in Figure 5 of Wang et al. (2014). To show that in the limiting case $n = 0.9$ reduced to a null line, we plot corresponding contours in the range $0.6 \leq n \leq 0.9$ on three preselected planes highlighted in panel (e). The size reduction of the contours with increasing n indicates the surface converging to a line. Such null lines are also conceptualized as favorable reconnection sites (Wang et al. 2014).

Region 4: Figure 5(f) shows magnetic field lines relevant to plasma rotation in B4. Notably, the null line from R3 intrudes

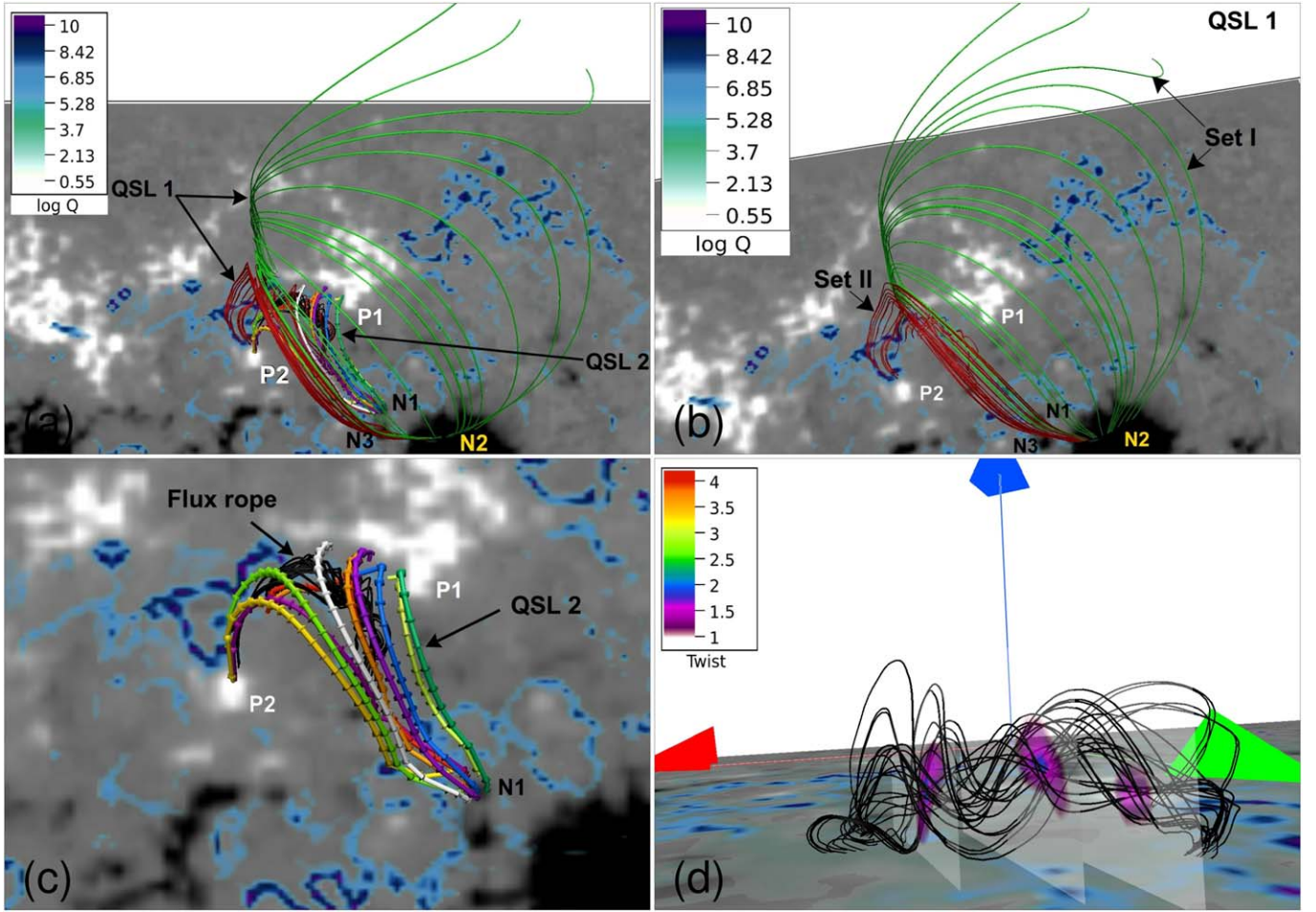


Figure 4. Panel (a) shows magnetic field line morphology of region R1 between positive and negative polarities P1, P2, N1, N2, and N3, respectively. Panel (b) highlights the structure of QSL1 composed of magnetic field lines in Set I (green) and Set II (maroon). Panel (c) shows the zoomed-in top view of the flux-rope structure (black) and an overlying QSL2 (multicolor arrowed magnetic field lines), between the positive and negative polarities P1, P2, and N1, respectively. Panel (d) shows the side view of the flux rope, where three vertical planes along the cross section of the flux rope show the twist value T_w at different locations along the flux rope. In all the panels the $\log Q$ between 5 and 10 is overlaid on the B_z -component of the magnetogram at the bottom boundary.

into R4, and the extreme left plane in R3 (Figure 5(e)) is also shared by R4.

4. HMHD and MHD Simulations of NOAA AR 12734

4.1. Governing Equations and Numerical Model

In the spirit of our earlier related works (Prasad et al. 2018, 2020; Nayak et al. 2019), the plasma is idealized to be incompressible and thermodynamically inactive, as well as explicitly nonresistive. While this relatively simple idealization is naturally limited, it exposes the basic dynamics of magnetic reconnections unobscured by the effects due to compressibility and heat transfer. Although the latter are important for coronal loops (Ruderman & Roberts 2002), they do not directly affect the magnetic topology—the focus of this paper. Historically rooted in classical hydrodynamics, such idealizations have a proven record in theoretical studies of geo/astrophysical phenomena (Rossby 1938; Dahlburg et al. 1991; Bhattacharyya et al. 2010; Bora et al. 2021). Inasmuch as their cognitive value depends on an a posteriori validation against the observations, the present study offers yet another opportunity to do so.

The Hall forcing has been incorporated (Bora et al. 2021) in the computational model EULAG-MHD (Smolarkiewicz & Charbonneau 2013) to solve the dimensionless HMHD

equations,

$$\frac{\partial \mathbf{v}}{\partial t} + (\mathbf{v} \cdot \nabla) \mathbf{v} = -\nabla p + (\nabla \times \mathbf{B}) \times \mathbf{B} + \frac{1}{R_F^A} \nabla^2 \mathbf{v}, \quad (7)$$

$$\frac{\partial \mathbf{B}}{\partial t} = \nabla \times (\mathbf{v} \times \mathbf{B}) - d_H \nabla \times ((\nabla \times \mathbf{B}) \times \mathbf{B}), \quad (8)$$

$$\nabla \cdot \mathbf{v} = 0, \quad (9)$$

$$\nabla \cdot \mathbf{B} = 0, \quad (10)$$

where $R_F^A = (v_A L / \nu)$ (ν being the kinematic viscosity) is an effective fluid Reynolds number, having the plasma speed replaced by the Alfvén speed v_A . Hereafter R_F^A is denoted as fluid Reynolds number for convenience. The transformation of the dimensional quantities (expressed in cgs units) into the corresponding nondimensional quantities,

$$\begin{aligned} \mathbf{B} &\longrightarrow \frac{\mathbf{B}}{B_0}, \mathbf{x} \longrightarrow \frac{\mathbf{x}}{L_0}, \mathbf{v} \longrightarrow \frac{\mathbf{v}}{v_A}, \\ t &\longrightarrow \frac{t}{\tau_A}, p \longrightarrow \frac{p}{\rho_0 v_A^2}, \end{aligned} \quad (11)$$

assumes arbitrary B_0 and L_0 , while the Alfvén speed $v_A \equiv B_0 / \sqrt{4\pi \rho_0}$. Here ρ_0 is a constant mass density, and d_H is the

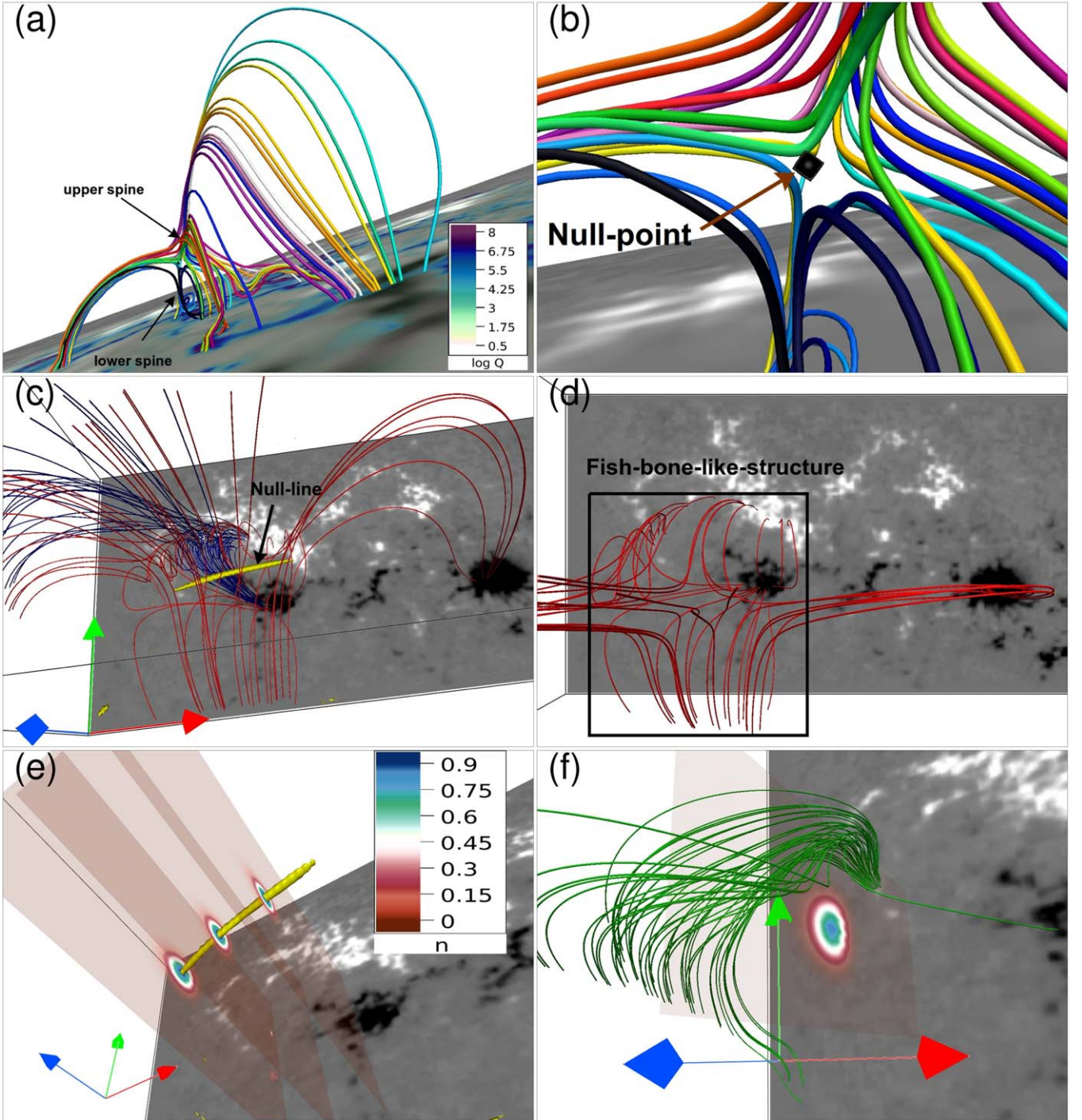


Figure 5. Panel (a) shows a 3D null spine-fan configuration in region R2, with B_z as the bottom boundary overlaid with $\log Q$ between 5 and 10. Panel (b) is the zoomed-in view of panel (a), highlighting the 3D null point (in black)—with an isosurface of $n = 0.6$ indicated by an arrow. Panel (c) shows the side view of magnetic field line structure in region R3, along with the yellow surface representing the null line corresponding to $n = 0.9$. Panel (d) shows the top-down view of red magnetic field lines of panel (c) forming a fish-bone-like structure. In panel (e) we show the value of n on three different vertical planes passing through the cross sections of the null-line surface. Notably, the planes show circles in the cross section at different locations, which indicates that the yellow surface is a null line. Panel (f) depicts magnetic field line morphology in region R4, along with the value of n on a vertical plane, where the green circular contour corresponds to $n = 0.6$, suggesting that the right part of magnetic field line morphology may be a part of the null-line geometry (shown in panel (c)).

Hall parameter. In the limit of $d_H = 0$, Equations (7)–(9) reduce to the MHD equations (Prasad et al. 2018).

The governing Equations (7)–(9) are numerically integrated using EULAG-MHD—an MHD extension (Smolarkiewicz & Charbonneau 2013) of the established Eulerian/Lagrangian comprehensive fluid solver EULAG (Prusa et al. 2008) predominantly used in atmospheric research. The EULAG

solvers are based on the spatio-temporally second-order-accurate nonoscillatory forward-in-time advection scheme MPDATA (for *multidimensional positive-definite advection transport algorithm*; Smolarkiewicz 2006). Importantly, unique to MPDATA is its widely documented dissipative property mimicking the action of explicit subgrid-scale turbulence models wherever the concerned advective field is underresolved, the property known

Table 1
Salient Features of Magnetic Field Line Dynamics in R1

Magnetic Field Line Structure	HMHD	MHD
QSL1	Fast reconnection followed by a significant rise of loops, eventually reconnecting higher in the corona.	Slow reconnection followed by a limited rise of loops.
QSL2	Fast reconnection causing the magnetic field lines to entirely disconnect from the polarity P2.	Due to slow reconnection, magnetic field lines remain connected to P2.
Flux rope	Fast slipping reconnection of the flux-rope footpoints, followed by the expansion and rise of the rope envelope.	Slow slipping reconnection and rise of the flux-rope envelope; the envelope does not reach the QSL1.

as implicit large-eddy simulations (ILES; Margolin et al. 2006). In effect, magnetic reconnections resulting in our simulations dissipate the under-resolved magnetic field along with other advective field variables and restore the flux freezing. These reconnections, being intermittent and local, successfully mimic physical reconnections.

4.2. Numerical Setup

The simulations are carried out by mapping the physical domain of $256 \times 128 \times 128$ pixels on the computational domain of $x \in \{-1, 1\}$, $y \in \{-0.5, 0.5\}$, $z \in \{-0.5, 0.5\}$ in a Cartesian coordinate system. The dimensionless spatial step sizes are $\Delta x = \Delta y = \Delta z \approx 0.0078$. The dimensionless time step is $\Delta t = 5 \times 10^{-4}$, set to resolve whistler speed—the fastest speed in incompressible HMHD. The rationale is briefly presented in the Appendix. The corresponding initial state is motionless ($\mathbf{v} = 0$), and the initial magnetic field is provided from the non-FFF extrapolation. The nonzero Lorentz force associated with the extrapolated field pushes the magnetofluid to initiate the dynamics. Since the maximal variation of magnetic flux through the photosphere is only 2.28% of its initial value during the flare (not shown), the B_z at the bottom boundary (at $z = 0$) is kept fixed throughout the simulation, while all other boundaries are kept open. For velocity, all boundaries are set open. The mass density is set to $\rho_0 = 1$.

The fluid Reynolds number is set to 500, which is roughly two orders of magnitude smaller than its coronal value $\approx 25,000$ (calculated using kinematic viscosity $\nu = 4 \times 10^9 \text{ m}^2 \text{ s}^{-1}$ (Aschwanden 2005) in solar corona). Without any loss in generality, the reduction in R_F^A can be envisaged to cause a reduction in computed Alfvén speed, $v_A|_{\text{computed}} \approx 0.02 \times v_A|_{\text{corona}}$, where the L for the computational and coronal length scales are set to 71 and 100 Mm, respectively. This diminished Alfvén speed reduces the requirement of computational resources and also relates it to the observation time. The results presented herein pertain to a run for $1200\Delta t$ that, along with the normalizing $\tau_A \approx 3.55 \times 10^3 \text{ s}$, roughly corresponds to an observation time of ≈ 35 minutes. For the ease of reference in comparison with observations, we present the time in units of $0.005\tau_A$ (which is 17.75 s) in the discussions of the figures in subsequent sections.

Although the coronal plasma idealized to have reduced Reynolds number is inconsequential here, in a comparison of MHD and HMHD evolution, we believe that the above rationale merits further contemplation. Undeniably such a coronal plasma is not a reality. Nevertheless, the reduced R_F^A does not affect the reconnection or its consequence but slows down the dynamics between two such events and, importantly, reduces the computational cost, making data-based simulations

realizable even with reasonable computing resources. A recent work by Jiang et al. (2016) used a homologous approach toward simulating a realistic and self-consistent flaring region.

In the present simulations, all parameters are identical for the MHD and the HMHD except for the d_H , respectively set to 0 and 0.004. The value 0.004 is motivated by recognizing ILES dissipation models intermittent magnetic reconnections at the $\mathcal{O}(\|\Delta \mathbf{x}\|)$ length scales, consistent with the thesis put forward in Introduction, we specify an appreciable Hall coefficient as $d_H = 0.5\Delta z/L \approx 0.004$, where $L = 1 \equiv$ smallest extent of the computational volume, having $\Delta y = \Delta z \approx 0.0078$ as the dissipation scales because of the ILES property of the model. Correspondingly, the value is also at the lower bound of the pixel or scale order approximation and, in particular, an order of magnitude smaller than its coronal value valid at the actual dissipation scale. An important practical benefit of this selection is the optimization of the computational cost while keeping magnetic field line dynamics tractable. Importantly, with dissipation and Hall scales being tied, an increased current density at the dissipation scale introduces additional slippage of field lines in HMHD over MHD (due to the Hall term) and may be responsible for more effective and faster reconnections found in the Hall simulation reported below.

4.3. Comparison of the HMHD and MHD Simulations

The simulated HMHD and MHD dynamics leading to the flare show unambiguous differences. This section documents these differences by comparing methodically simulated evolution of the magnetic structures and topologies in NOAA AR 12734—namely, the flux rope, QSLs, and null points—identified in the extrapolated initial data in regions R1–R4.

4.3.1. Region R1

The dynamics of region R1 are by far the most complex among the four selected regions. To facilitate future reference, as well as to outline the organization of the discussion that follows, Table 1 provides a brief summary of our findings—in a spirit of theses to be proven by the simulation results.

The global dynamics of magnetic field lines in region R1 is illustrated in Figure 6; consult Figure 4 for the initial condition and terminology. The snapshots from the HMHD and MHD simulations are shown in panels (a)–(d) and (e)–(f), respectively. In panels (a) and (b), corresponding to $t = 19$ and $t = 46$, the footpoints of magnetic field lines in Set II (near P2, marked maroon) exhibit slipping reconnection along high values of the squashing factor Q indicated by black arrows. Subsequently, between $t = 80$ and 81 in panels (c) and (d), the magnetic field lines in Set II rise in the corona and reconnect with magnetic field lines in Set I to change connectivity. The MHD

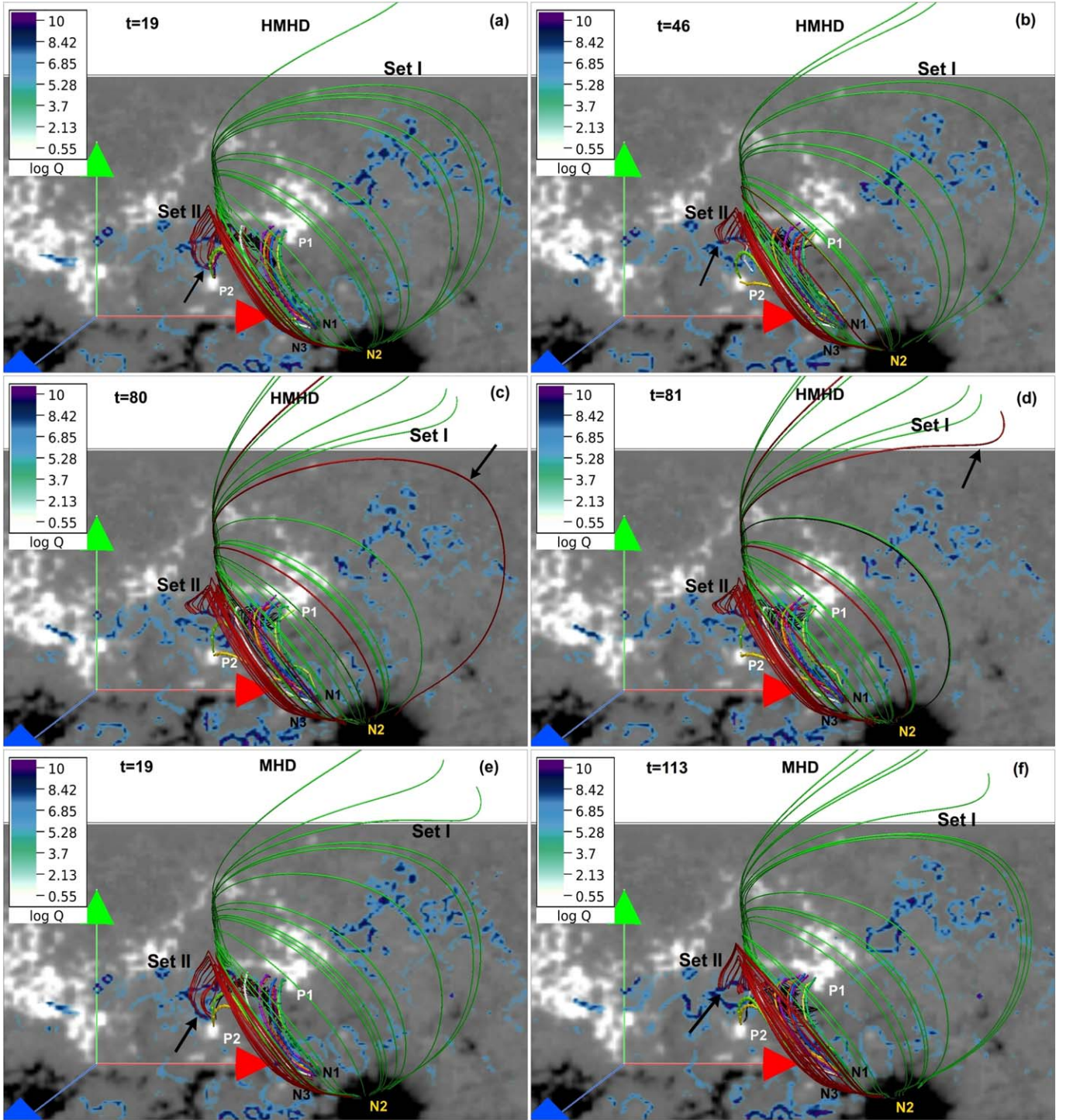


Figure 6. Snapshots of the global dynamics of magnetic field lines in region R1 during the HMHD and MHD simulations are shown in panels (a)–(d) and (e)–(f), respectively. Panels (a) and (b) show the departure of footpoints of magnetic field lines in Set II (maroon) away from polarity P2 between $t = 19$ and 46 on the bottom boundary (marked by black arrow). Panel (c) depicts the rising magnetic field lines in Set II (maroon) higher up in the solar corona at $t = 80$ (marked by black arrow), and panel (d) shows subsequent connectivity change of rising magnetic field lines at $t = 81$, due to reconnection with the Set I (green) magnetic field lines. Panels (e) and (f) depict the departure of footpoints of magnetic field lines in Set II (maroon) away from P2 between $t = 19$ and 113, which is similar to the HMHD but delayed in time—indicating the slower dynamics in the MHD. Notably, significant rise of magnetic field lines in Set II and consequent reconnection of it with magnetic field lines in Set I higher up in the solar corona are absent in the MHD simulation. An animation of this figure is available. The video shows the evolution of magnetic field lines in region R1 from $t = 0$ to 109 for the HMHD and from $t = 0$ to 120 for the MHD simulations, respectively. The real-time duration of the video is 12 s.

(An animation of this figure is available.)

counterpart of the slipping reconnection in panels (e) and (f) corresponds to magnetic field lines in Set II between $t = 19$ and 113. It lags behind the HMHD displays, thus implying slower

dynamics. Furthermore, the magnetic field lines in Set II, unlike for the HMHD, do not reach up to the magnetic field lines in Set I constituting QSL1 and hence do not reconnect. A

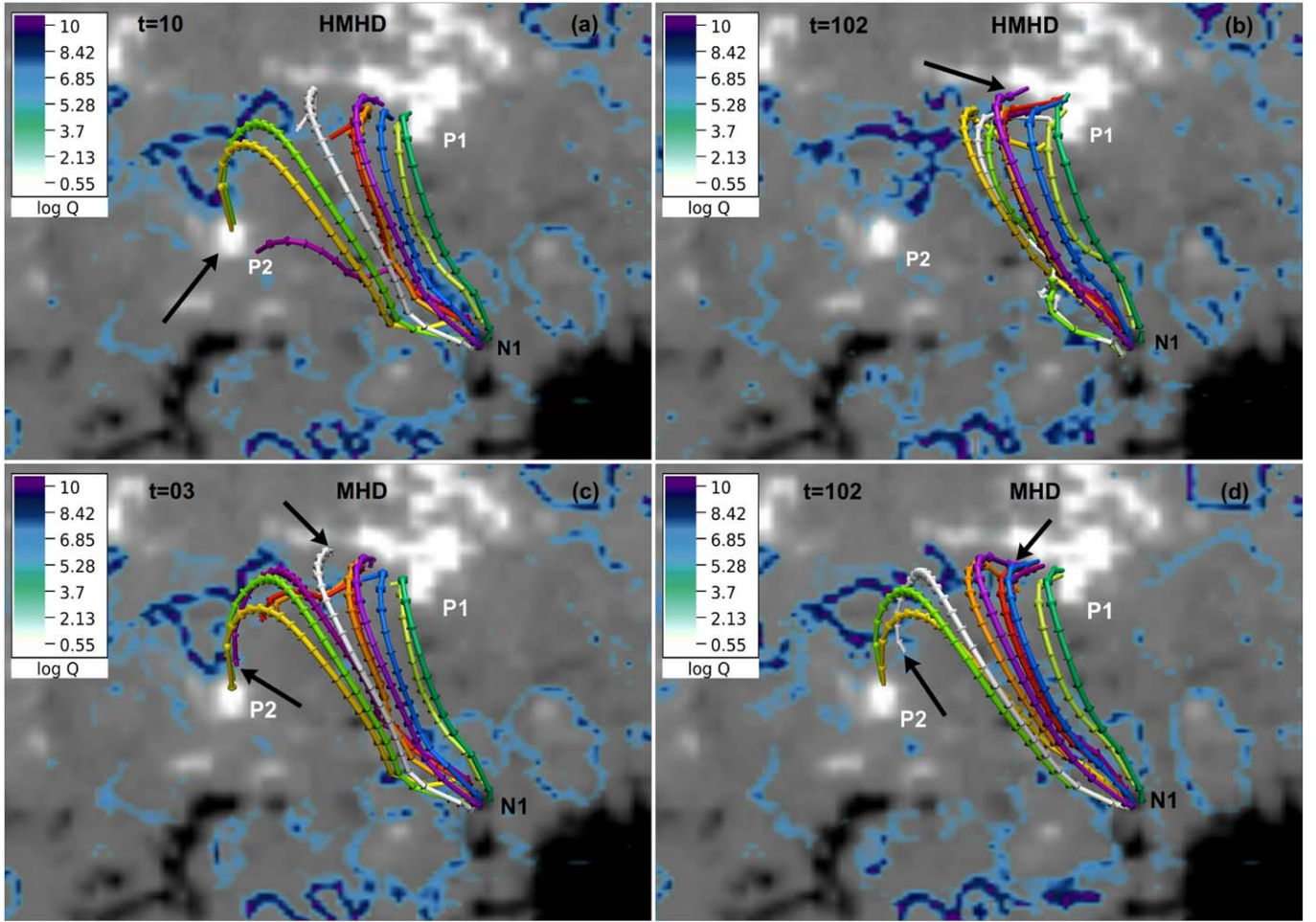


Figure 7. Snapshots of the HMHD and MHD evolution of QSL2 (Figure 4(c)) are shown in panels (a)–(b) and (c)–(d), respectively. Panels (a)–(b) show that magnetic field lines anchored in the positive polarity P2 at $t = 10$ have moved to the polarity P1 by $t = 102$ and changed their connectivity (marked by black arrow) owing to reconnection along QSL during the HMHD. Panels (c)–(d) show the connectivity changes of the violet and white color magnetic field lines during the MHD evolution. The white field line was initially connecting the polarities P1 and N1, whereas the violet field line was connecting P2 and N1. As a result of reconnection along QSL, the white field line changes its connectivity from P1 to P2, and the violet field line changes the connectivity from P2 to P1 (marked by black arrows). Notably, unlike the HMHD simulation, not all magnetic field lines move to P1 from P2 owing to reconnection along QSL during the MHD, which indicates the slower dynamics. An animation of this figure is available. The video shows the evolution of QSL2 (shown in Figure 4) in region R1 from $t = 0$ to 120 for the HMHD and MHD simulations, respectively. The real-time duration of the video is 12 s.

(An animation of this figure is available.)

more informative visualization of the highlighted dynamics is supplemented in an online animation. The decay index is calculated for each time instant for both the simulations and is found to be less than 1.5 above the flux rope, indicating an absence of the torus instability (Kliem & Török 2006). For more detail, Figures 7 and 8 illustrate the evolution of QSL2 and flux rope separately.

Panels (a)–(b) and (c)–(d) of Figure 7 show, respectively, the instants from the HMHD and MHD simulations of QSL2 between P1, P2, and N1. The HMHD instants show that magnetic field lines that were anchored between P2 and N1 at $t = 10$ have moved to P1 around $t = 102$, marked by black arrows in both panels. The magnetic field lines anchored at P2 moved to P1 along the high Q values—signifying the slipping reconnection. The MHD instants in panels (c)–(d) show the connectivity changes of the violet and white colored magnetic field lines. The white field line was initially connecting P1 and N1, whereas the violet field line was connecting P2 and N1. As a result of reconnection along QSL, the white field line changed its connectivity from P1 to P2, and the violet field line changes

the connectivity from P2 to P1 (marked by black arrows). Notably, in contrast to the HMHD evolution, all magnetic field lines initially anchored in P2 do not change their connectivity from P2 to P1 during the MHD evolution, indicating the slower dynamics.

The flux rope has been introduced in panels (c) and (d) of Figure 4, respectively, below the QSL2 and in enlargement. Its HMHD and MHD evolutions, along with the twists on three different vertical cross sections, are shown in panels (a)–(f) and (g)–(i) of Figure 8, respectively. Magnetic field lines constituting the rope rise substantially higher during the HMHD evolution as a result of slipping reconnection along the high Q in panels (c)–(f). In panel (c) at $t = 32$, the footpoints of the rope that are anchored on the right side (marked by the black arrow) change their connectivity from one high Q regime to another in panel (d) at $t = 33$, i.e., the footpoints on the right have moved to the left side (marked by the black arrow). Afterward, the magnetic field lines rise because of the continuous slipping reconnection, as evidenced in panels (e)–(f) and the supplemented animation. Comparing panel (a) with

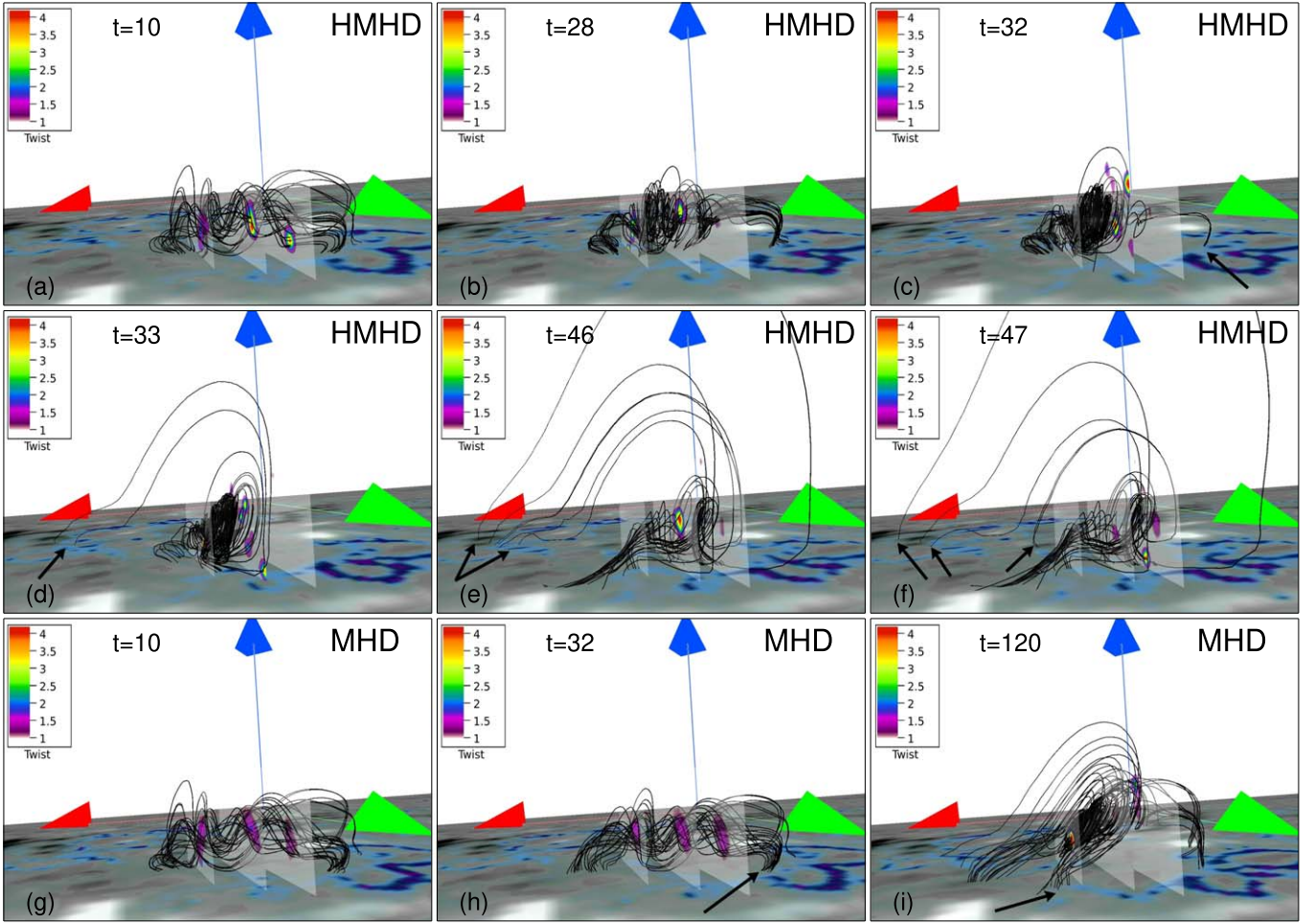


Figure 8. Time sequence showing the HMHD (panels (a)–(f)) and MHD (panels (g)–(i)) evolution of the flux rope (shown in Figure 4(c)), along with the twist T_w . Panel (a) shows that the twist on the middle and the right plane on flux rope is higher than initial values (see Figure 4(d)) and reduced with time in panel (b). Panels (c)–(d) depict the connectivity change of the footpoint of the rope from right to left (indicated by the black arrow) due to reconnection along QSL. Panels (e)–(f) show the connectivity change of magnetic field lines on left-hand side (indicated by the black arrow). Panels (g)–(i) depict the dynamic rise of the flux rope between $t = 10$ and 120 during the MHD simulation. Notably, the footpoints of the rope on the right side (marked by the black arrow) at $t = 32$ in panel (h) have moved toward left by $t = 120$ in panel (i) as a result of reconnection along QSL. An animation of this figure is available. The video shows the evolution of magnetic flux rope in region R1 from $t = 0$ to 92 for the HMHD simulations and from $t = 0$ to 120 for the MHD simulations. The real-time duration of the video is 12 s.

(An animation of this figure is available.)

panel (g) at $t = 10$ and panel (c) with panel (h) at $t = 32$, we note that the twist value T_w is higher in the HMHD simulation. Panels (h)–(i) highlight the displaced footpoints of the flux rope due to slipping reconnection at $t = 32$ and 120 (see the black arrow). The rope is preserved throughout the HMHD and MHD simulations.

The rise and expansion of the flux-rope envelope owing to slipping reconnection are remarkable in the HMHD simulation. Dudík et al. (2014) have already shown such a flux-rope reconnection along QSL in a J-shaped current region, with slipping reconnection causing the flux rope to form a sigmoid (S-shaped hot channel observed in EUV images of SDO/AIA) followed by its rise and expansion. Further insight is gained by overlaying the flux-rope evolution shown in Figure 8 with direct volume rendering of $|\mathbf{J}|/|\mathbf{B}|$ (Figures 9 and 10) as a measure of magnetic field gradient for the HMHD and MHD simulations. In the HMHD case, the appearance of large values of $|\mathbf{J}|/|\mathbf{B}| > 475$ inside the rope (panels (a)–(c)) and footpoints on the left of the rope (panels (d)–(e)) are apparent. The development of the large $|\mathbf{J}|/|\mathbf{B}|$ is indicative of reconnection

within the rope. Contrarily, MHD simulation lacks such high values of $|\mathbf{J}|/|\mathbf{B}|$ in the same time span (panels (a)–(b)), and the field lines show no slippage—agreeing with the proposal that large currents magnify the Hall term, resulting in more effective slippage of field lines.

4.3.2. Region R2

To compare the simulated magnetic field lines dynamics in region R2 with the observed tip of the W-shaped flare ribbon B2 (Figure 3(a)) during the HMHD and MHD evolution, we present the instants from both simulations at $t = 70$ in panels (a) and (b) of Figure 11, respectively. Importantly, the lower spine remains anchored to the bottom boundary during the HMHD simulation (evident from the supplemented animation along with Figure 11). Further, Figure 12 shows the evolution of the lower spine along with the $|\mathbf{J}|/|\mathbf{B}|$ on the bottom boundary for the HMHD (panels (a)–(d)) and MHD (panels (e)–(h)) cases. In the HMHD case, noteworthy is the slipping motion of the lower spine (marked by the black arrows) tracing the $|\mathbf{J}|/|\mathbf{B}| > 350$ regions on the

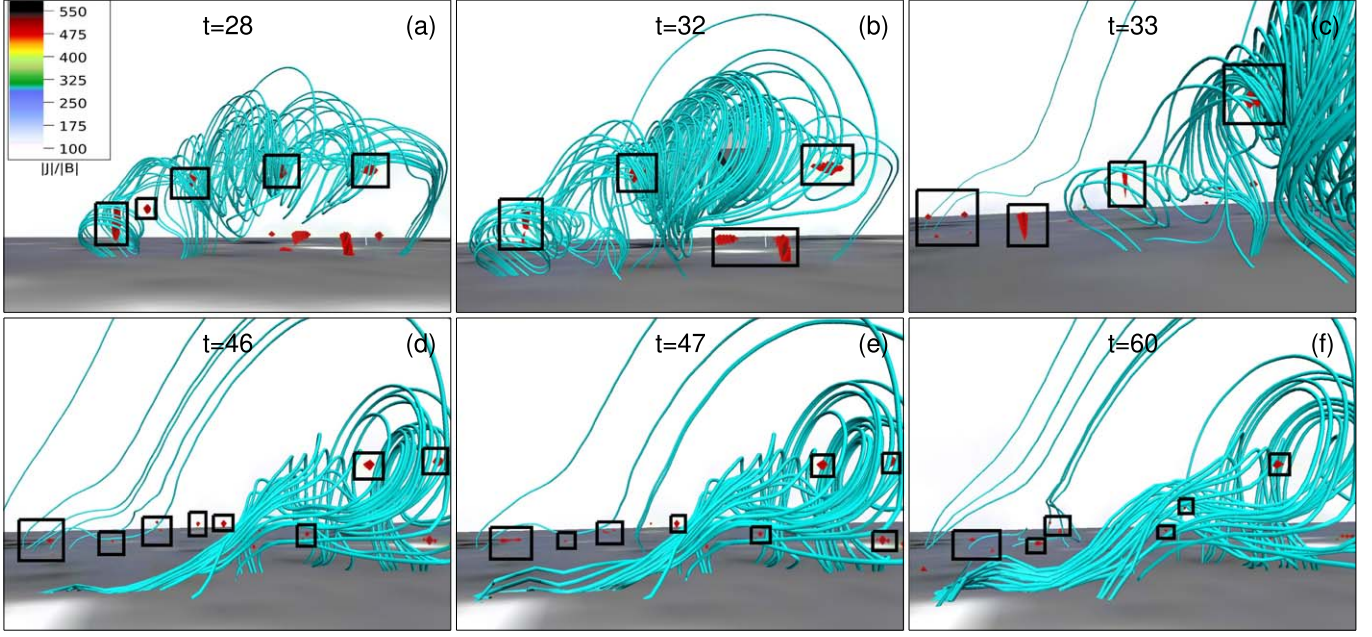


Figure 9. Temporal variation of the direct volume rendering of $(|J|/|B|)$ along with the flux rope is shown during the HMHD simulation. Noticeably, the high magnetic field gradient regions with $(|J|/|B|) \geq 475$ develop within (panels (a)–(c)) and on the left side of the flux rope (panels (d)–(f)). The values $(|J|/|B|) \geq 475$ in each panel are enclosed within the black rectangular boxes. The color of flux rope has been changed to cyan to show $(|J|/|B|)$ values in region R1.

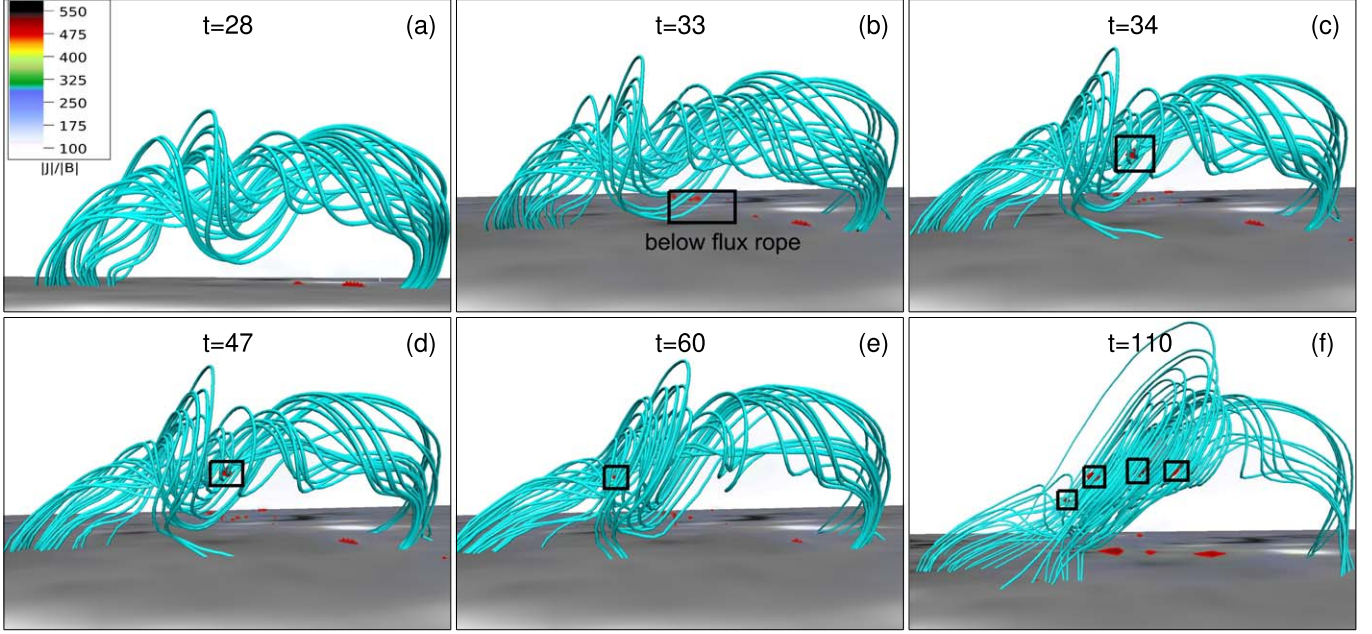


Figure 10. Temporal variation of the direct volume rendering of $(|J|/|B|)$ along with the flux rope is shown during the MHD simulation. Panels (a) and (b) show the absence of high values of $(|J|/|B|)$ within the rope at $t = 28$ and 32 , but in later panels (c)–(f) $(|J|/|B|) \geq 475$ appears (enclosed by the black rectangular boxes). Notably, as compared to the HMHD case (Figure 9), the development of $(|J|/|B|)$ is not significant in region R1 during the MHD. The color of flux rope has been changed to cyan to show $(|J|/|B|)$ values in region R1.

bottom boundary (panels (a)–(b)), whereas in the MHD such high values of $|J|/|B|$ are absent on the bottom boundary—suggesting that the slippage of the field lines on the bottom boundary is less effective compared to the HMHD. The finding is in agreement with the idea of enhanced slippage of field lines due to high current densities as conceptualized in the introduction. The anchored lower spine provides a path for the plasma to flow downward to the brightening segment B2. In

the actual corona, such flows result in flare brightening (Benz 2017). In contrast, the lower spine gets completely disconnected from the bottom boundary (Figure 11(b)) in the MHD simulation, hence failing to explain the tip of the W-shaped flare ribbon in B2. The anchored lower spine in the HMHD simulation is caused by a complex series of magnetic field line reconnections at the 3D null and along the QSLs in R2, as depicted in the animation.

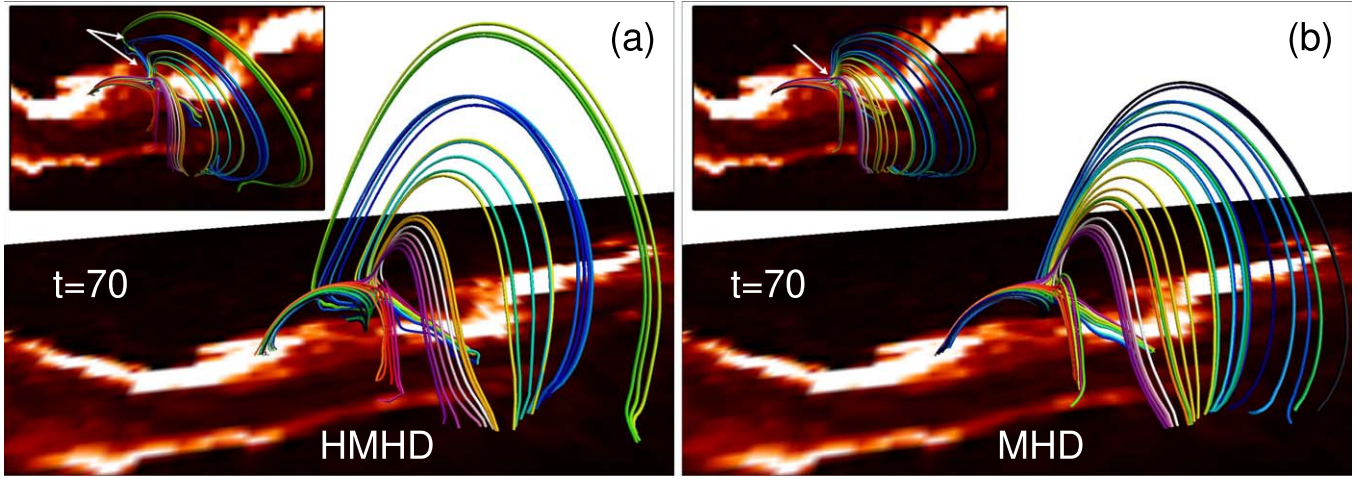


Figure 11. Panels (a) and (b) show the comparison of magnetic field line topology in region R2 at $t = 70$ with the flare ribbons observed in the SDO/AIA 304 Å channel (side views) during the HMHD and MHD simulations, respectively. The inset images in the upper left corner in each panel show the top view of the same magnetic field line topology. Notably, the spine is anchored in the HMHD, while it is not connected to the bottom boundary in the MHD at $t = 70$ (marked by the white arrow in inset images). An animation of this figure is available. The video shows the evolution of magnetic field lines in region R2 with the AIA 304 Å image at the bottom boundary from $t = 0$ to 117 for the HMHD simulations and from $t = 0$ to 120 for the MHD simulations. The real-time duration of the video is 12 s. (An animation of this figure is available.)

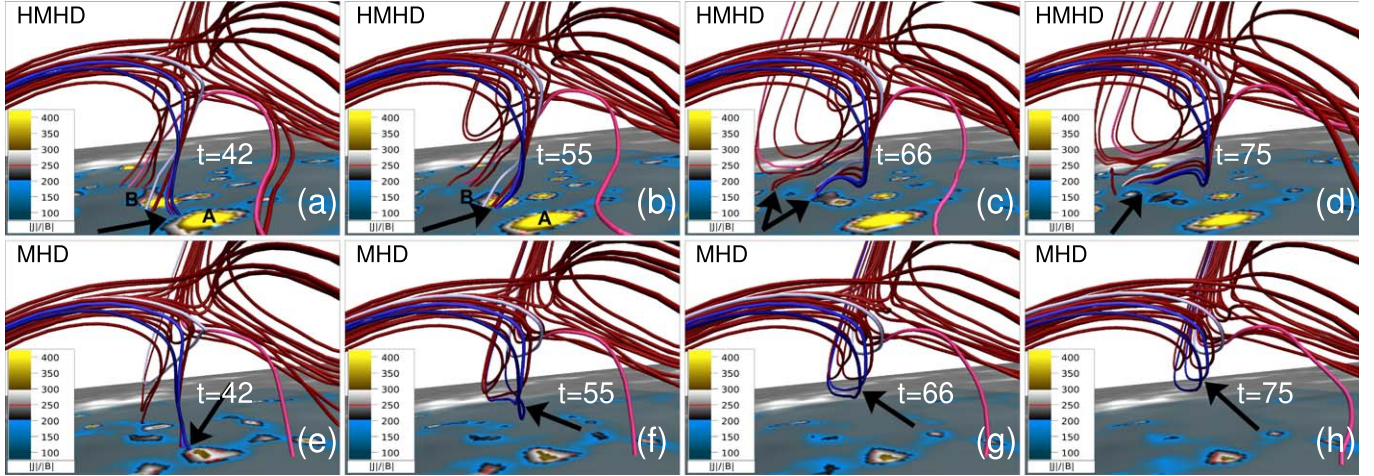


Figure 12. Panels (a)–(d) depict the slipping motion of the lower spine field lines (also shown in the Figure 5 but the color of field lines has been changed) overlaid with the $|J|/|B|$ on the bottom boundary during the HMHD evolution. The motion is marked by the black arrows in all the panels, indicating the successive change in the location of field lines on the bottom boundary. A and B (in panels (a) and (b)) are the two regions with $|J|/|B| > 350$ on the bottom boundary (just below the lower spine). Notably, the field lines follow the high values of $|J|/|B|$ on the bottom boundary and remain anchored. Panels (e)–(h) show the evolution of the same lower spine field lines during the MHD simulation. The large values of $|J|/|B|$ do not appear below the lower spine (on the bottom boundary), and it does not remain anchored from $t \approx 55$ onward (panels (f)–(h)).

4.3.3. Region R3

HMHD and MHD simulations of magnetic field lines dynamics around the null line are shown in Figures 13 and 14, respectively. Figure 13 shows the blue magnetic field lines prior to and after the reconnections (indicated by black arrows) between $t = 4$ and 5 (panels (a)–(b)), between $t = 52$ and 53 (panels (c)–(d)), and between $t = 102$ and 103 (panels (e)–(f)) during the HMHD simulation. Figure 14 shows the same blue magnetic field lines prior to and after the reconnections (indicated by black arrows) between $t = 12$ and 13 (panels (a)–(b)), between $t = 59$ and 60 (panels (c)–(d)), and between $t = 114$ and 115 (panels (e)–(f)) during the MHD simulation. Comparison of panels (a)–(f) of Figure 13 with the same panels of Figure 14 reveals earlier reconnections of the blue magnetic field lines in the HMHD simulation. In both figures, green velocity vectors on the right represent the local plasma

flow. They get aligned downward along the footpoints of the fan magnetic field lines, as reconnection progresses. Consequently, the plasma flows downward and impacts the denser and cooler chromosphere to give rise to the brightening in B3. The velocity vectors pointing upward represent a flow toward the null line. The plasma flow pattern in R3 is the same in the HMHD and MHD simulations. The vertical y - z plane passing through the cross section of the null-line surface (also shown in Figure 5(d)) in all the panels of Figures 13 and 14 shows the variation of n with time. It is evident that the null is not destroyed throughout the HMHD and MHD evolution. Structural changes in the field lines caused by reconnection are nearly identical for both the simulations, indicating inefficacy of the Hall term. This inefficacy is justifiable, as $|J|/|B|$ remains small ≈ 10 (not shown) in both HMHD and MHD evolution.

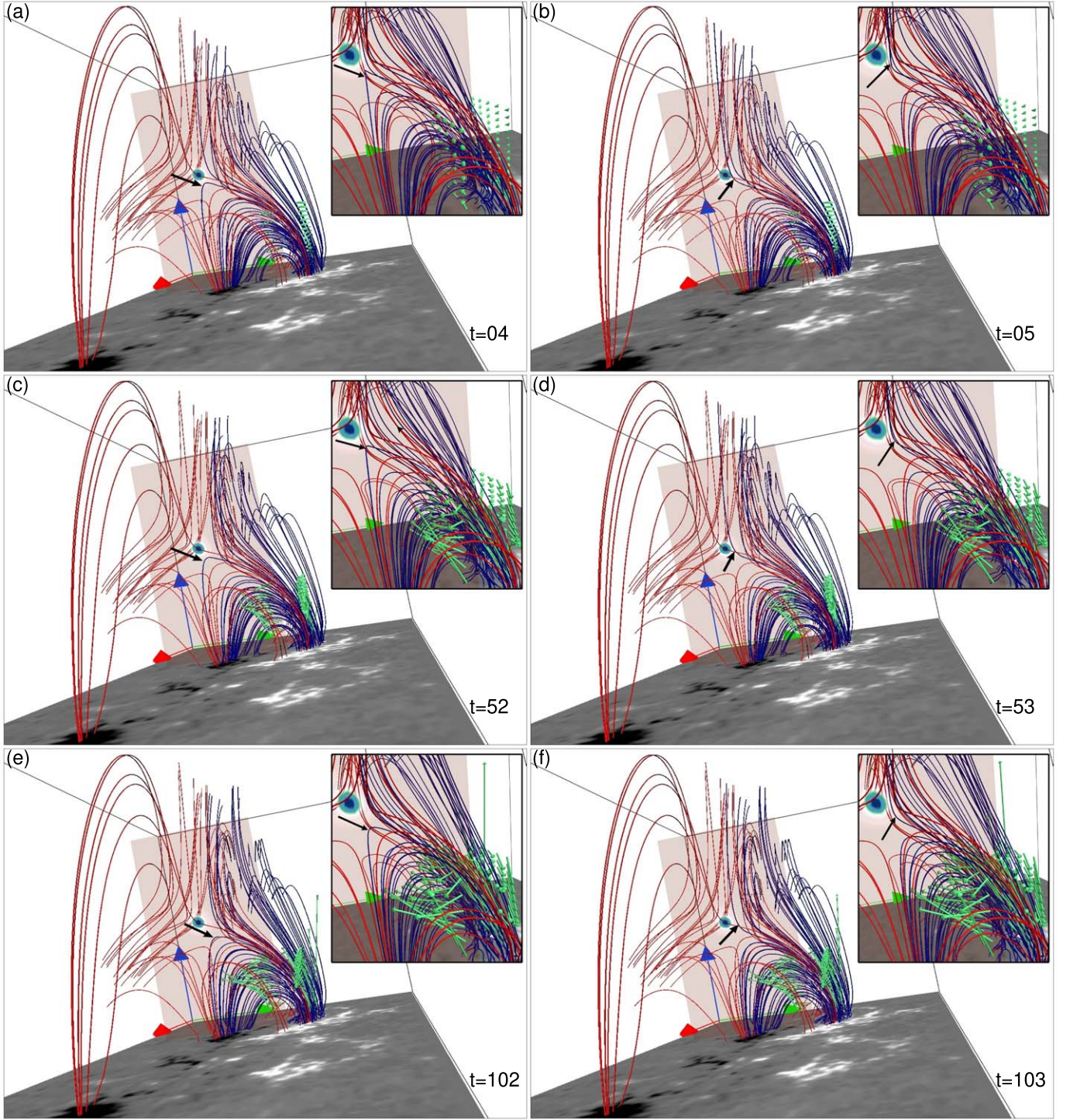


Figure 13. Time sequence showing the blue field line prior to and after reconnection (indicated by the black arrow) in region R3 during the HMHD simulation. Evolution of the flow vectors is depicted by green arrows (on the right side)—mimicking the direction of the plasma flow. The plane along the cross section of magnetic field line morphology in R3, showing the blue circular contours, represents the value of n (also shown in Figure 5(d)).

4.3.4. Region R4

The development of the circular motion of magnetic field lines in region R4 during the HMHD simulation is depicted in Figure 15. It shows the global dynamics of magnetic field lines in R4, and the inset images show the zoomed-in view of magnetic field lines in R4 to highlight the circular motion of magnetic field lines. The bottom boundary is B_z in the main figure, while the

inset images have the z -component of the plasma flow at the bottom boundary (on the x - y plane). The red vectors represent the plasma flow direction and magnitude in all the panels of Figure 15, where the counterclockwise pattern of the plasma flow is evident. The global dynamics highlight reconnection of the loop anchored between positive and negative polarities at $t = 60$ in Figure 15 as it gets disconnected from the bottom boundary in panels (c)–(d) of Figure 15. The animation accompanying

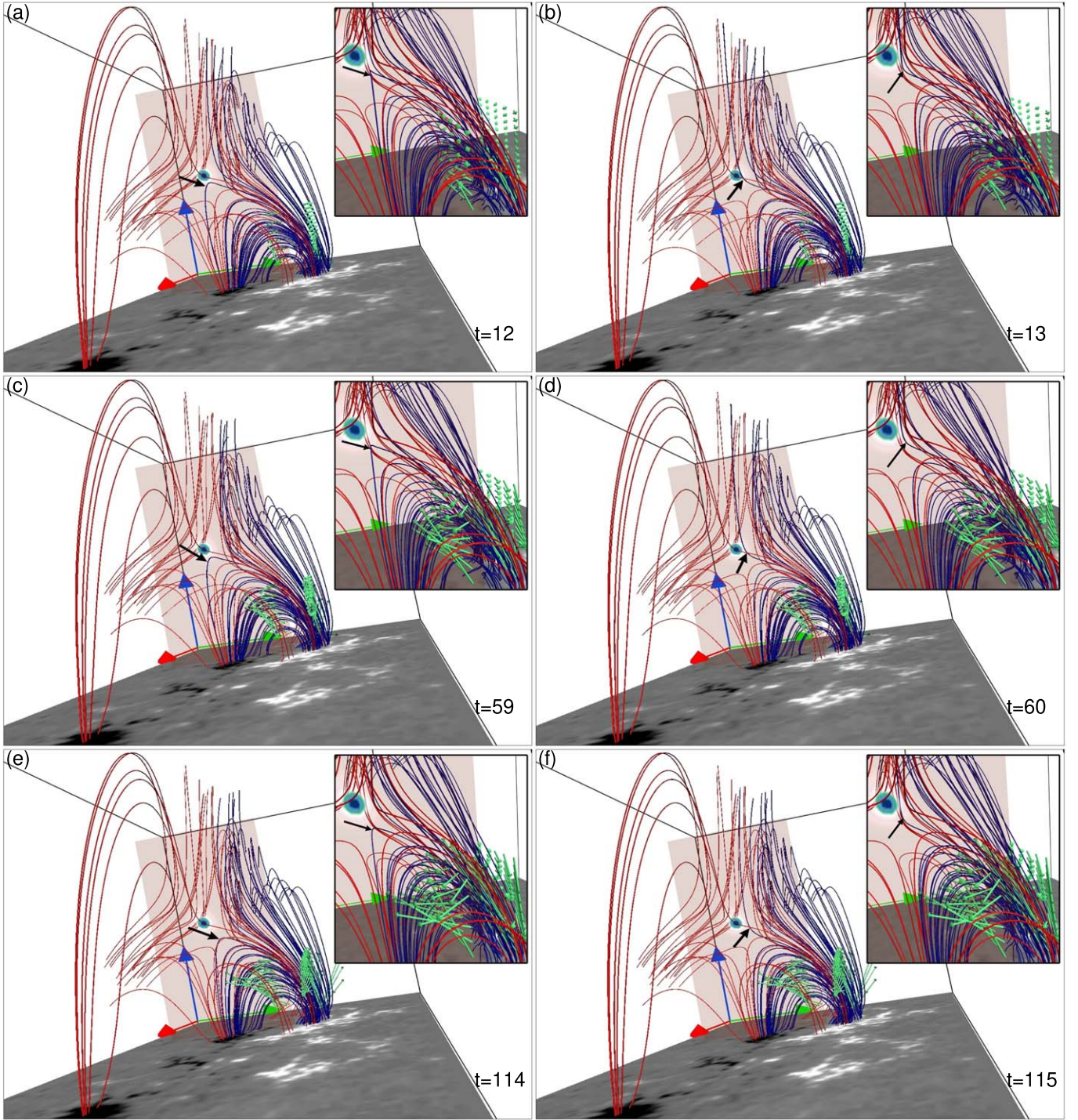


Figure 14. Time sequence showing the blue field line prior to and after reconnection (indicated by the black arrow) in region R3 during the MHD simulation. Evolution of the flow vectors is depicted by green arrows (on the right side)—mimicking the direction of the plasma flow. The plane along the cross section of magnetic field line morphology in R3, showing the blue circular contours, represents the value of n (also shown in Figure 5(d)). Notably, reconnection of the blue magnetic field lines is slightly delayed in comparison to its HMHD counterpart. A combined animation of Figure 13 and this figure is available. The video shows the evolution of magnetic field lines of region R3 along with the flow vectors (green) from $t = 0$ to 120 for the HMHD and MHD simulations, respectively. The real-time duration of the video is 12 s.

(An animation of this figure is available.)

Figure 15 highlights a counterclockwise motion of footpoints in the same direction as the plasma flow, indicating that field lines are frozen in the fluid. The trapped plasma may cause the rotating structure B4 in the observations (see Figure 3(a)). However, no such motion is present during the MHD evolution of the same

magnetic field lines (not shown). An interesting feature noted in the animation is the clockwise slippage of field lines after the initial counterclockwise rotation. Further analysis of R4 using the direct volume rendering of $|\mathbf{J}|/|\mathbf{B}|$ is presented in Figure 16. The figure shows that $|\mathbf{J}|/|\mathbf{B}|$ attains high values ≥ 225 (enclosed by

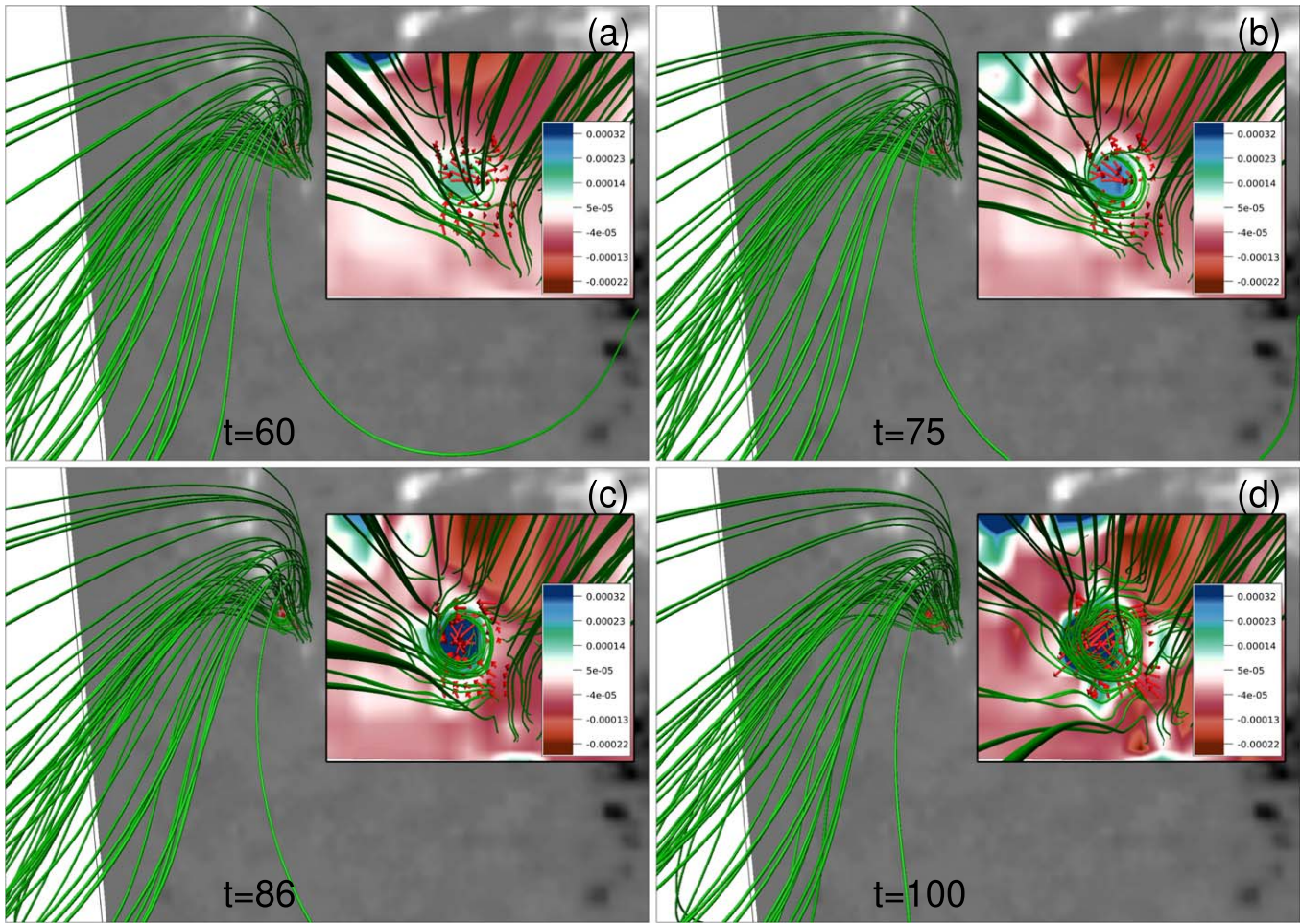


Figure 15. Panels (a)–(d) show the global dynamics of magnetic field lines in region R4 during the HMHD simulation. Inset images in each panel (on the right) depict the time sequence of the zoomed top-down view of the rotational motion of magnetic field lines. The background shows the variation of the z -component of flow $\in [-0.00022, 0.00032]$ in all inset images. The red vectors represent the plasma flow and change its direction in a counterclockwise manner in panels (a)–(d). The rotational motion of magnetic field lines coincides with the circular part of the flow. An animation of this figure is available. The video shows the evolution of magnetic field lines in region R4 from $t = 0$ to 100 for the HMHD simulation. The development of a counterclockwise rotational motion of the footpoints from $t \approx 33$ onward and the clockwise slippage of the field line from $t \approx 76$ onward are evident in the video. The real-time duration of the video is 10 s.

(An animation of this figure is available.)

the blue rectangles) within the rotating field lines from $t \approx 86$ onward. This suggests that the slippage of field lines is, once again, related to the high magnetic field gradients.

For completeness, we present the snapshots of an overall magnetic field line morphology including the magnetic structures and topology of regions R1, R2, R3, and R4 together, overlaid with 304 and 171 Å from the HMHD and MHD simulations. Figure 17(a) shows an instant (at $t = 75$) from the HMHD simulation where the topologies and magnetic structures in R1, R2, R3, and R4, plus the additionally drawn locust color magnetic field lines between R2 and R3, are shown collectively. It shows an excellent match of the magnetic field lines in R2 with the observed tip of the W-shaped flare ribbon at B2, which is pointed out by the pink arrow in panel (a). Footpoints of the spine-fan geometry around the 3D null orient themselves in the same fashion as the observed tip of the W-shaped flare ribbon at B2 as seen in the 304 Å channel of SDO/AIA. The rising loops indicated by the white arrow correspond to the same evolution as shown in Figure 6. The overall magnetic field line morphology mentioned in Figure 15(a) is given at the same time ($t = 75$) during the MHD simulation overlaid with the 304 Å image in Figure 15(b).

Importantly, unlike the HMHD simulation, the MHD simulation does not account for the anchored lower spine and fan magnetic field lines of the 3D null at the center of the B2. Also, the significant rise of the overlying maroon magnetic field lines and the circular motion of the material in B4 are captured in the HMHD simulation only. In panel (c) magnetic field lines overlaid with the 171 Å image show that the magnetic field lines (higher up in the solar atmosphere) have resemblance with the post-flare loops during the HMHD. Overall, the HMHD evolution seems to be in better agreement with the observations in comparison to the MHD evolution.

5. Summary and Discussion

This paper compares data-based HMHD and MHD simulations using the flaring NOAA AR 12734 as a test bed. The importance of the HMHD stems from the realization that the Hall term in the induction equation cannot be neglected in the presence of the magnetic reconnection—the underlying cause of solar flares. The selected event is the C1.3 class flare on 2019 March 8 around 03:19 UT for the aforementioned comparison. Although the event is analyzed and reported in the

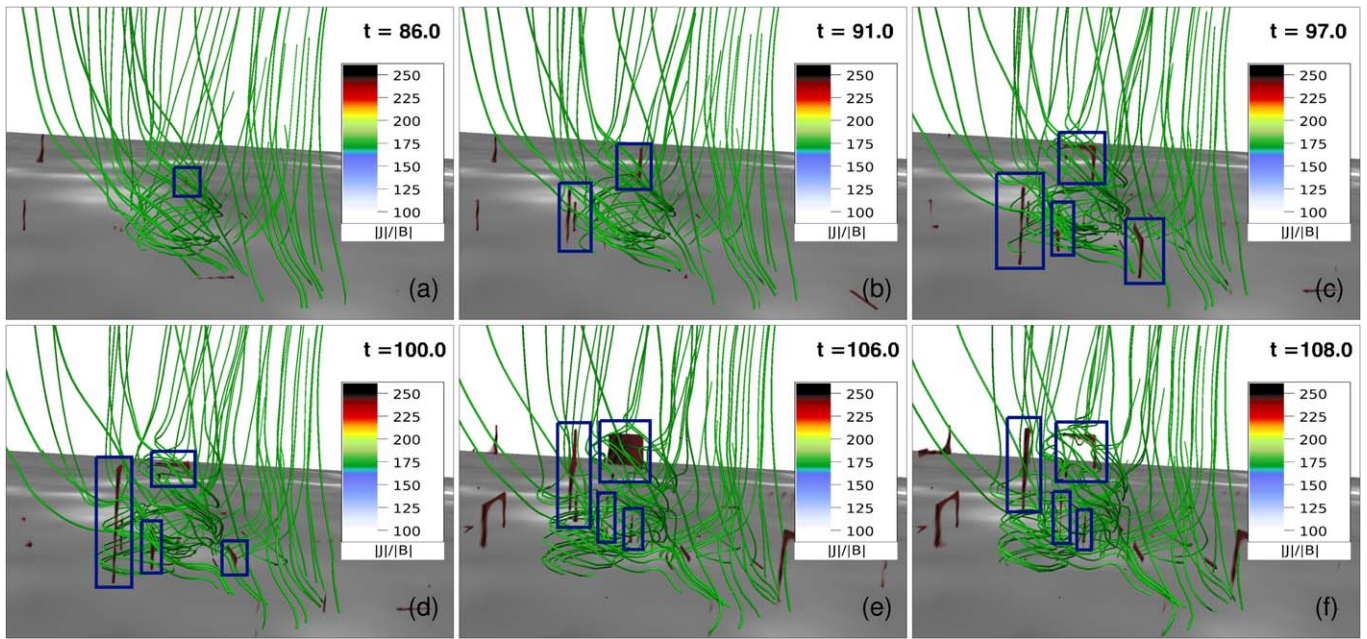


Figure 16. Panels (a)–(f) show the side view of the rotating magnetic field line structure in region R4 overlaid with $|J|/|B|$. The figure depicts the temporal development of strong magnetic field gradient regions of $|J|/|B| > 225$ (enclosed in the blue rectangular boxes) within the rotating magnetic structure.

literature, it is further explored using the multiwavelength observations from SDO/AIA. The identified important features are an elongated EUV counterpart of the eruption on the western side of the AR and a W-shaped flare ribbon and circular motion of cool chromospheric material on the eastern part. The magnetic field line dynamics near these features are utilized to compare the simulations. Notably, the simulations idealize the corona to have an Alfvén speed that is two orders of magnitude smaller than its typical value. Congruent to the general understanding, the Hall parameter is selected to tie the Hall dynamics to the dissipation scale $\mathcal{O}(\Delta x)$ in the spirit of the ILES carried out in the paper. The magnetic reconnection here is associated with the slippage of magnetic field lines from the plasma parcels, effective at the dissipation scale due to local enhancement of magnetic field gradient. The same enhancement also amplifies the Hall contribution, presumably enhancing the slippage and thereby making the reconnection faster and more effective than the MHD.

The coronal magnetic field is constructed by extrapolating the photospheric vector magnetic field obtained from the SDO/HMI observations employing the non-FFF technique (Hu et al. 2010). The concentrated distribution of the Lorentz force on the bottom boundary and its decrease with the height justify the use of non-FFF extrapolation for the solar corona. The initial nonzero Lorentz force is also crucial in generating self-consistent flows that initiate the dynamics and cause the magnetic reconnections. Analyses of the extrapolated magnetic field reveal several magnetic structures and topologies of interest: a flux rope on the western part at the flaring location, a 3D null point along with the fan-spine configuration at the center, and a “fish-bone-like structure” surrounding the null line on the eastern part of the AR. All of these structures are found to be cospatial with the observed flare ribbon brightening.

The HMHD simulation shows faster slipping reconnection of the flux-rope footpoints and overlying magnetic field lines (constituting QSLs above the flux rope) at the flaring location.

Consequently, the overlying magnetic field lines rise, eventually reaching higher up in the corona and reconnecting to provide a path for plasma to eject out. The finding is in agreement with the observed elongated EUV counterpart of the eruption on the western part of the AR. Contrarily, such a significant rise of the flux rope and overlying field lines to subsequently reconnect higher up in the corona is absent in the MHD simulation—signifying that the reconnection is slower compared to the HMHD. Intriguingly, rise and expansion of the flux rope and overlying field lines due to slipping reconnection on QSLs have also been modeled and observed in an earlier work by Dudík et al. (2014). These are typical features of the “standard solar flare model in 3D,” which allows for a consistent explanation of events that are not causally connected (Dudík et al. 2014). It also advocates that null points and true separatrices are not required for the eruptive flares to occur—concurring with the results of this work. HMHD evolution of the fan-spine configuration surrounding the 3D null point is in better agreement with the tip of the W-shaped flare ribbon at the center of the AR. The lower spine and fan magnetic field lines remain anchored to the bottom boundary throughout the evolution, which can account for the plasma flowing downward after the reconnection and cause the brightening, whereas in the MHD the lower spine gets disconnected and cannot account for the brightening. The reconnection dynamics around the null line and the corresponding plasma flow direction are the same in the HMHD and MHD simulations and agree with the observed brightening. Nevertheless, reconnection is earlier in the HMHD. HMHD evolution captures an anticlockwise circular motion of magnetic field lines in the left part of the AR that is cospatial with the location of the rotating chromospheric material on the eastern side of the AR. No such motion was found in the MHD simulation. Importantly, the simulations explicitly associate generation of large magnetic field gradients with HMHD compared to MHD, resulting in faster and more efficient field line slippage because of the enhanced Hall term.

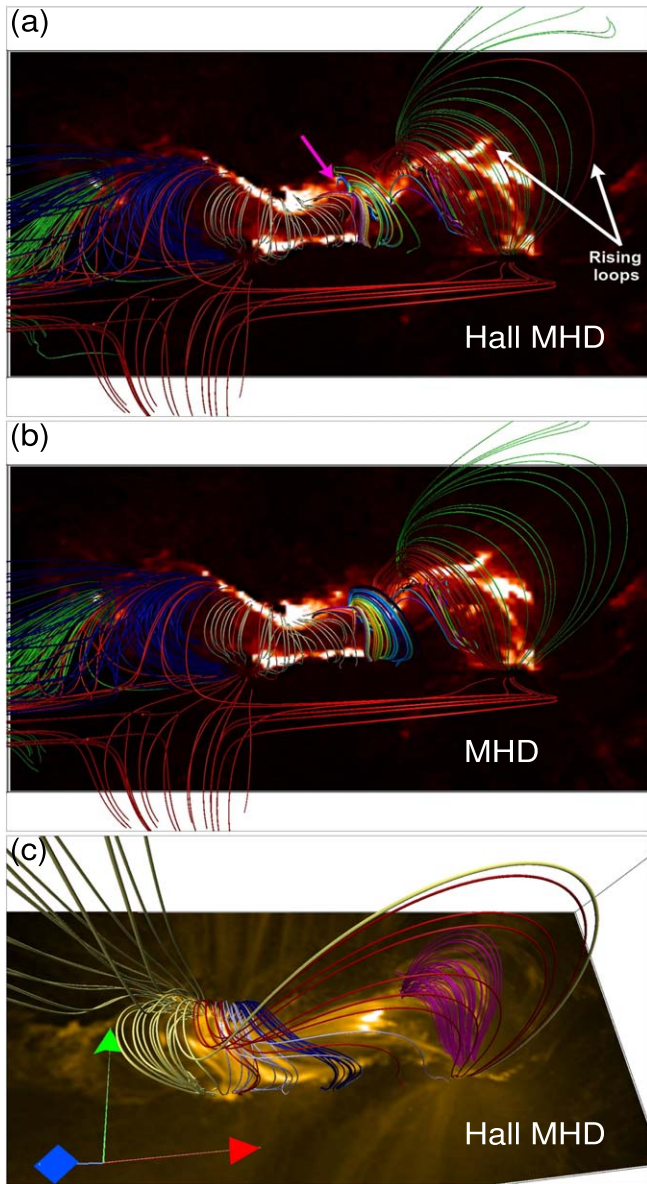


Figure 17. Top-down view of an overall magnetic field line morphology overlaid on the SDO/AIA 304 Å (panels (a) and (b)) and 171 Å images (panel (c)). Anchored magnetic field line footpoints in the central part match well with the observed tip of the W-shaped flare ribbon (marked by the pink arrow in panel (a)) in the HMHD, while magnetic field line footpoints are completely disconnected from the bottom boundary in the MHD (panel (b)). Loops rising higher up in the corona are remarkable in the HMHD (indicated by the white arrow in panel (a)). An animation of panels (a) and (b) is available. The video shows the evolution of magnetic field lines in AR along with the AIA 304 Å image at the bottom from $t = 0$ to 120 for the HMHD and MHD simulations, respectively. The real-time duration of the video is 12 s.

(An animation of this figure is available.)

Overall, the results documented in the paper show that the HMHD explains the flare brightening better than the MHD, prioritizing the requirement to include HMHD in future state-of-the-art data-based numerical simulations.

The authors thank the anonymous referee for providing insightful comments and suggestions that increased the scientific content of the paper. The simulations are performed using the 100TF cluster Vikram-100 at Physical Research Laboratory, India. We wish to acknowledge the visualization

software VAPOR (www.vapor.ucar.edu), for generating relevant graphics. Q.H. and A.P. acknowledge partial support of NASA grants 80NSSC17K0016, 80NSSC21K1671, L.W.S. 80NSSC21K0003 and NSF awards AGS-1650854 and AGS-1954503. This research was also supported by the Research Council of Norway through its Centres of Excellence scheme, project No. 262622, as well as through the Synergy grant No. 810218 (ERC-2018-SyG) of the European Research Council.

Appendix

The dimensionless time step is obtained by employing the Hall induction equation

$$\frac{\partial \mathbf{B}}{\partial t} = -d_H \nabla \times ((\nabla \times \mathbf{B}) \times \mathbf{B}), \quad (\text{A1})$$

for a stationary fluid. The aforementioned equation is linearized over an equilibrium magnetic field \mathbf{B}_0 to obtain

$$\frac{\partial \delta \mathbf{B}}{\partial t} = -d_H [\nabla \times (\nabla \times \delta \mathbf{B}) \times \mathbf{B}_0], \quad (\text{A2})$$

$\delta \mathbf{B}$ being the perturbation. To obtain the wave modes, the perturbation is assumed to be periodic along x and y of a Cartesian coordinate system

$$\delta \mathbf{B}_x = \delta \mathbf{B}_y \propto \exp[i(k_z z - \omega t)], \quad (\text{A3})$$

where the equilibrium field is selected as $\mathbf{B}_0 = B_0 \hat{e}_z$. Straightforward mathematical manipulations yield the dispersion relation for the Whistler wave as

$$\omega = d_H B_0 k_z^2. \quad (\text{A4})$$

The wavenumber is selected as $k_z = (2\pi)/\Delta z$, where Δz is the dissipation scale in the computational domain, making the choice harmonious with the philosophy used extensively in the paper. Since the dimensionless $\rho_0 = 1$ in the numerical model, Equation (A4) can be written as

$$\left(\frac{\Delta z}{\Delta t}\right)_{\text{whis}} = 4\pi^{\frac{3}{2}} d_H \left(\frac{\Delta z}{\Delta t}\right)_{\text{Alf}} \left(\frac{1}{\Delta z}\right)_{\text{whis}}. \quad (\text{A5})$$

Where $\Delta z_{\text{whis}} = \Delta z_{\text{Alfvén}} = 0.0078$, the dissipation scale in the present model along with $d_H = 0.004$, while $\Delta t_{\text{Alf}} \approx 10^{-3}$ from previous numerical experiments; suggest $\Delta t = \Delta t_{\text{whis}} \approx 10^{-4}$ in the present model.

ORCID iDs

K. Bora <https://orcid.org/0000-0002-3402-273X>
R. Bhattacharyya <https://orcid.org/0000-0003-4522-5070>
Avijeet Prasad <https://orcid.org/0000-0003-0819-464X>
Bhuwan Joshi <https://orcid.org/0000-0001-5042-2170>
Qiang Hu <https://orcid.org/0000-0002-7570-2301>

References

- Alfvén, H. 1942, *Natur*, **150**, 405
- Amari, T., Canou, A., & Aly, J.-J. 2014, *Natur*, **514**, 465
- Aschwanden, M. J. 2005, *Physics of the Solar Corona. An Introduction with Problems and Solutions* (2nd ed.; Chichester: Praxis)
- Axford, W. I. 1984, *Geophysical Monograph Series*, Vol. 30 (Washington DC: American Geophysical Union), 1
- Benz, A. O. 2017, *LRS*, **14**, 2
- Bhattacharjee, A. 2004, *ARA&A*, **42**, 365
- Bhattacharyya, R., & Janaki, M. S. 2004, *PhPI*, **11**, 5615

- Bhattacharyya, R., Janaki, M. S., Dasgupta, B., & Zank, G. P. 2007, *SoPh*, **240**, 63
- Bhattacharyya, R., Low, B. C., & Smolarkiewicz, P. K. 2010, *PhPI*, **17**, 112901
- Birn, J., Drake, J. F., Shay, M. A., et al. 2001, *JGR*, **106**, 3715
- Bora, K., Bhattacharyya, R., & Smolarkiewicz, P. K. 2021, *ApJ*, **906**, 102
- Choudhuri, A. R. 1998, *The Physics of Fluids and Plasmas: An Introduction for Astrophysicists* (New York: Cambridge Univ. Press)
- Dahlburg, R. B., Antiochos, S. K., & Zang, T. A. 1991, *ApJ*, **383**, 420
- Démoulin, P. 2006, *AdSpR*, **37**, 1269
- Dudík, J., Janvier, M., Aulanier, G., et al. 2014, *ApJ*, **784**, 144
- Eyink, G. L., & Aluie, H. 2006, *PhyD*, **223**, 82
- Garcia, H. A. 1994, *SoPh*, **154**, 275
- Gary, G. A. 2001, *SoPh*, **203**, 71
- Hornig, G., & Schindler, K. 1996, *PhPI*, **3**, 781
- Hu, Q., & Dasgupta, B. 2008, *SoPh*, **247**, 87
- Hu, Q., Dasgupta, B., Choudhary, D. P., & Büchner, J. 2008, *ApJ*, **679**, 848
- Hu, Q., Dasgupta, B., Derosa, M. L., Büchner, J., & Gary, G. A. 2010, *JASTP*, **72**, 219
- Inoue, S., Hayashi, K., Magara, T., Choe, G. S., & Park, Y. D. 2014, *ApJ*, **788**, 182
- Jiang, C., & Feng, X. 2014, *SoPh*, **289**, 63
- Jiang, C., Feng, X., Wu, S. T., & Hu, Q. 2013, *ApJL*, **771**, L30
- Jiang, C., Wu, S. T., Feng, X., & Hu, Q. 2016, *NatCo*, **7**, 11522
- Joshi, B., Mitra, P. K., Bhattacharyya, R., et al. 2021, *SoPh*, **296**, 85
- Kliem, B., & Török, T. 2006, *PhRvL*, **96**, 255002
- Kumar, D., & Bhattacharyya, R. 2011, *PhPI*, **18**, 084506
- Kumar, S., Bhattacharyya, R., Dasgupta, B., & Janaki, M. S. 2017, *PhPI*, **24**, 082902
- Kumar, S., Bhattacharyya, R., Joshi, B., & Smolarkiewicz, P. K. 2016, *ApJ*, **830**, 80
- Kumar, S., Bhattacharyya, R., & Smolarkiewicz, P. K. 2015, *PhPI*, **22**, 082903
- Kumar, S., Nayak, S. S., Prasad, A., & Bhattacharyya, R. 2021, *SoPh*, **296**, 26
- Lazarian, A., & Vishniac, E. 2000, arXiv:astro-ph/0002067
- Lazarian, A., & Vishniac, E. T. 1999, *ApJ*, **517**, 700
- Lemen, J. R., Title, A. M., Akin, D. J., et al. 2012, *SoPh*, **275**, 17
- Liu, C., Prasad, A., Lee, J., & Wang, H. 2020, *ApJ*, **899**, 34
- Liu, R., Kliem, B., Titov, V., et al. 2016, *ApJ*, **818**, 148
- Mahajan, S. M., & Yoshida, Z. 1998, *PhRvL*, **81**, 4863
- Margolin, L. G., Rider, W. J., & Grinstein, F. F. 2006, *JTurb*, **7**, 15
- Mozar, F. S., Bale, S. D., & Phan, T. D. 2002, *PhRvL*, **89**, 015002
- Nayak, S. S., Bhattacharyya, R., Prasad, A., et al. 2019, *ApJ*, **875**, 10
- Nayak, S. S., Bhattacharyya, R., Smolarkiewicz, P. K., Kumar, S., & Prasad, A. 2020, *ApJ*, **892**, 44
- Parker, E. N. 1994, *Spontaneous Current Sheets in Magnetic Fields: With Applications to Stellar X-rays, Vol.1* (New York: Oxford Univ. Press), 1
- Parnell, C. E., Smith, J. M., Neukirch, T., & Priest, E. R. 1996, *PhPI*, **3**, 759
- Pesnell, W. D., Thompson, B. J., & Chamberlin, P. C. 2012, *SoPh*, **275**, 3
- Prasad, A., Bhattacharyya, R., Hu, Q., Kumar, S., & Nayak, S. S. 2018, *ApJ*, **860**, 96
- Prasad, A., Bhattacharyya, R., & Kumar, S. 2017, *ApJ*, **840**, 37
- Prasad, A., Dissauer, K., Hu, Q., et al. 2020, *ApJ*, **903**, 129
- Priest, E., & Forbes, T. 2000, *Magnetic Reconnection* (New York: Cambridge Univ. Press)
- Prusa, J. M., Smolarkiewicz, P. K., & Wyszogrodzki, A. A. 2008, *Comput. Fluids*, **37**, 1193
- Rossby, C. G. 1938, *Preface & Acknowledgments, Fluid Mechanics Applied to the Study of Atmospheric Circulations, Pt. I. Papers in Physical Oceanogr. & Met., Vol. VII* (Massachusetts: Cambridge and Woods Hole)
- Ruderman, M. S., & Roberts, B. 2002, *ApJ*, **577**, 475
- Sarp Yalim, M., Prasad, A., Pogorelov, N., Zank, G., & Hu, Q. 2020, arXiv:2007.12275
- Savcheva, A., Parlat, E., McKillop, S., et al. 2016, *ApJ*, **817**, 43
- Schindler, K., Hesse, M., & Birn, J. 1988, *JGR*, **93**, 5547
- Schou, J., Scherrer, P. H., Bush, R. I., et al. 2012, *SoPh*, **275**, 229
- Shi, C., Tenerani, A., Velli, M., & Lu, S. 2019, *ApJ*, **883**, 172
- Shibata, K., & Tanuma, S. 2001, *EP&S*, **53**, 473
- Smolarkiewicz, P. K. 2006, *IJNMF*, **50**, 1123
- Smolarkiewicz, P. K., & Charbonneau, P. 2013, *JCoPh*, **236**, 608
- Wang, H., Liu, C., Deng, N., et al. 2014, *ApJL*, **781**, L23
- Westerberg, L. G., & Åkerstedt, H. O. 2007, *PhPI*, **14**, 102905
- Wiegmann, T. 2008, *JGRA*, **113**, A03S02
- Wiegmann, T., Inhester, B., & Sakurai, T. 2006, *SoPh*, **233**, 215
- Wiegmann, T., & Sakurai, T. 2012, *LRSP*, **9**, 5